

# Regional Impact of Snow-Darkening on Snow Pack and the Atmosphere During a Severe Saharan Dust Deposition Event in Eurasia

Anika Rohde<sup>1</sup>, Heike Vogel<sup>2</sup>, Gholam Ali Hoshyaripour<sup>3</sup>, Christoph Kottmeier<sup>4</sup>, and Bernhard Vogel<sup>2</sup>

<sup>1</sup>Institute of Meteorology and Climate Research, Karlsruhe Institute of Technology

<sup>2</sup>Institute for Meteorology and Climate Research, Karlsruhe Institute of Technology

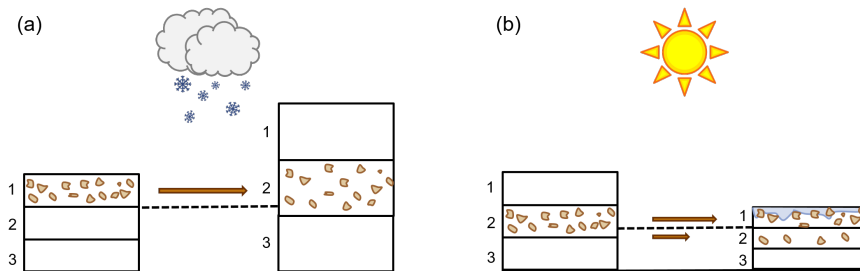
<sup>3</sup>Karlsruhe Institute of Technology

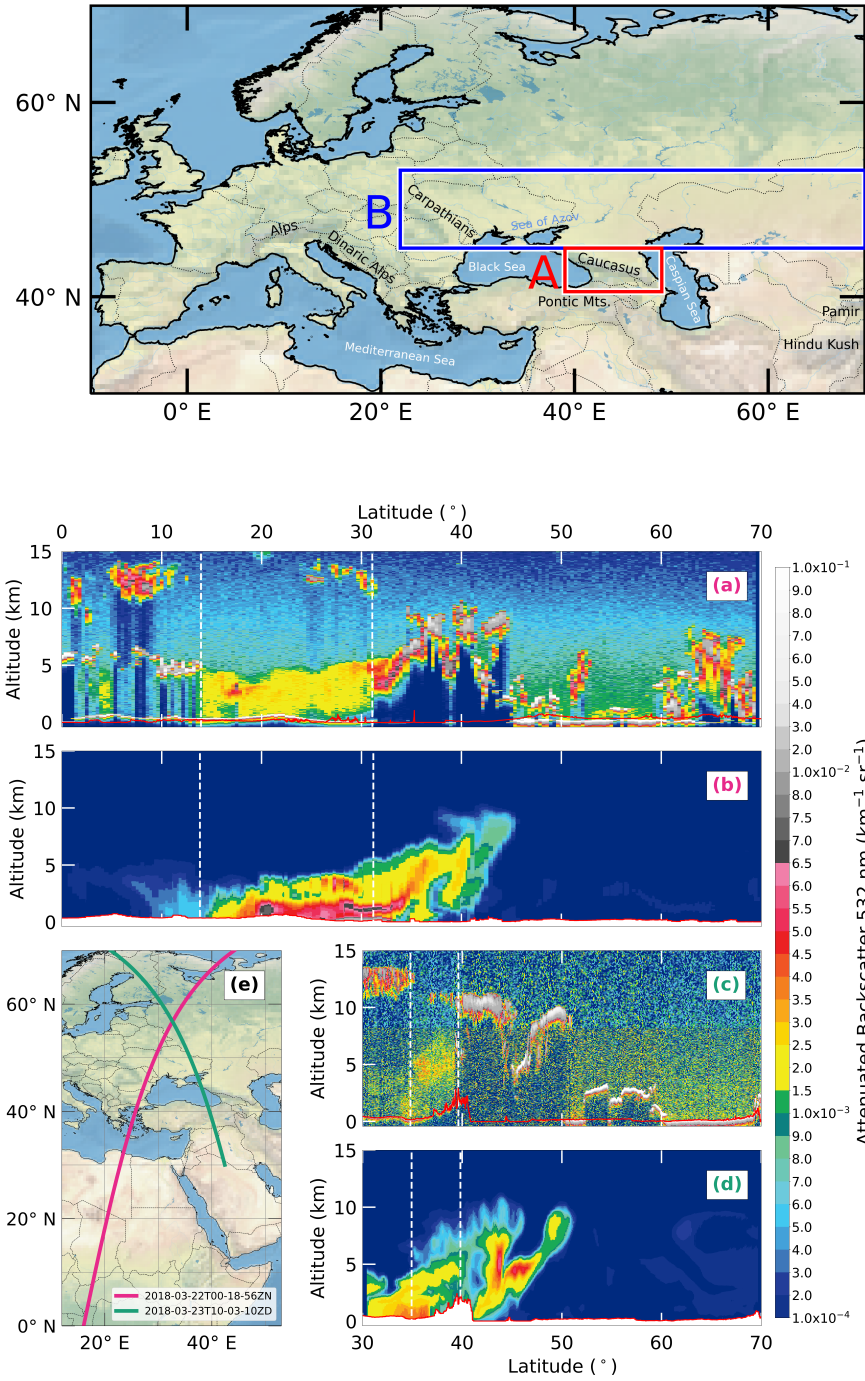
<sup>4</sup>Institut für Meteorologie und Klimaforschung, Universität / Forschungszentrum Karlsruhe

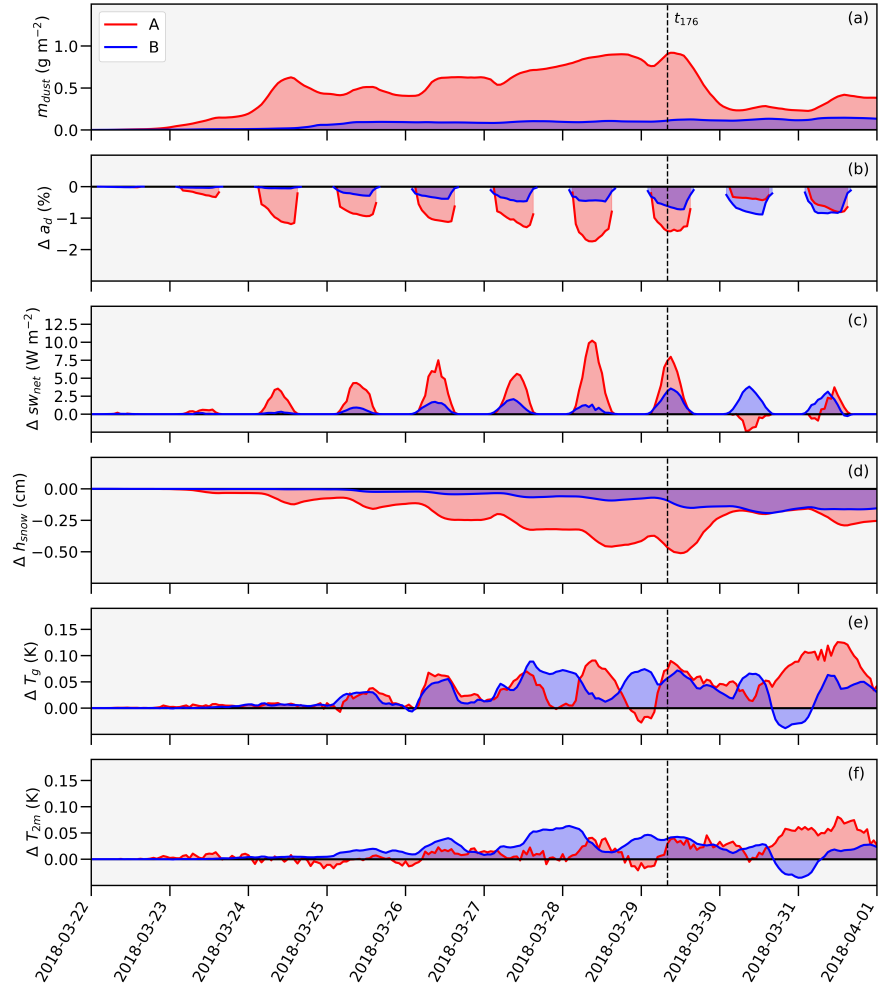
January 3, 2023

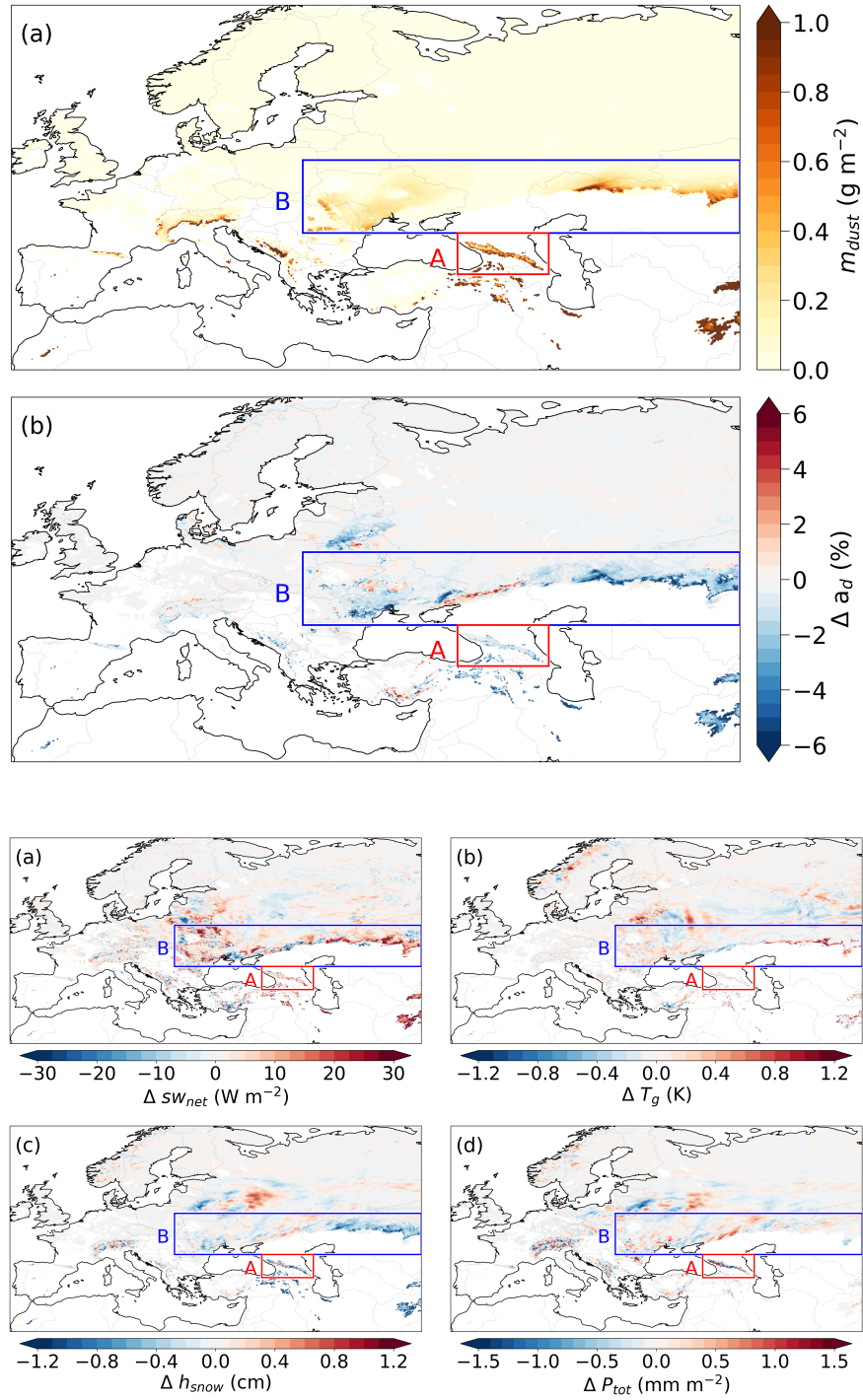
## Abstract

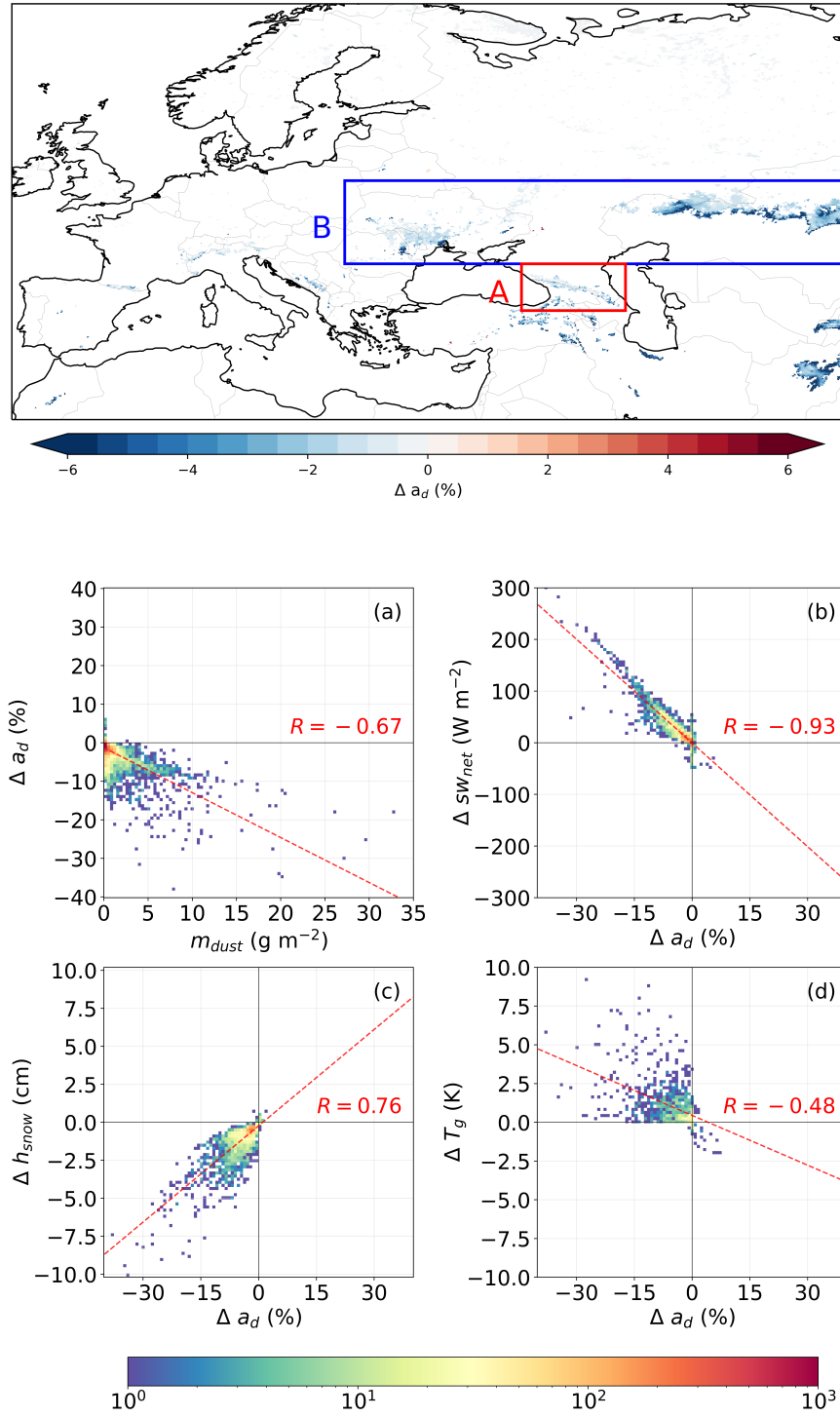
Light-absorbing impurities such as mineral dust can play a major role in reducing the albedo of snow surfaces. Particularly in spring, deposited dust particles lead to increased snow melt and trigger further feedbacks at the land surface and in the atmosphere. Quantifying the extent of dust-induced variations is difficult due to the high variability in the spatial distribution of mineral dust and snow. We present an extension of a fully coupled atmospheric and land surface model system to address the impact of mineral dust on the snow albedo across Eurasia. We evaluated the short-term effects of Saharan dust in a case study. To obtain robust results, we performed an ensemble simulation followed by statistical analysis. Mountainous regions showed a strong impact of dust deposition on snow depth. We found a mean significant reduction of -1.4 cm in the Caucasus Mountains after one week. However, areas with flat terrain near the snow line also showed strong effects despite lower dust concentrations. Here, the feedback to dust deposition was more pronounced as increase in surface temperature and air temperature. In the region surrounding the snow line, we found an average significant surface warming of 0.9 K after one week. This study shows that the impact of mineral dust deposition depends on several factors. Primarily, these are altitude, slope, snow depth, and snow cover fraction. Especially in complex terrain, it is therefore necessary to use fully coupled models to investigate the effects of mineral dust on snow pack and the atmosphere.

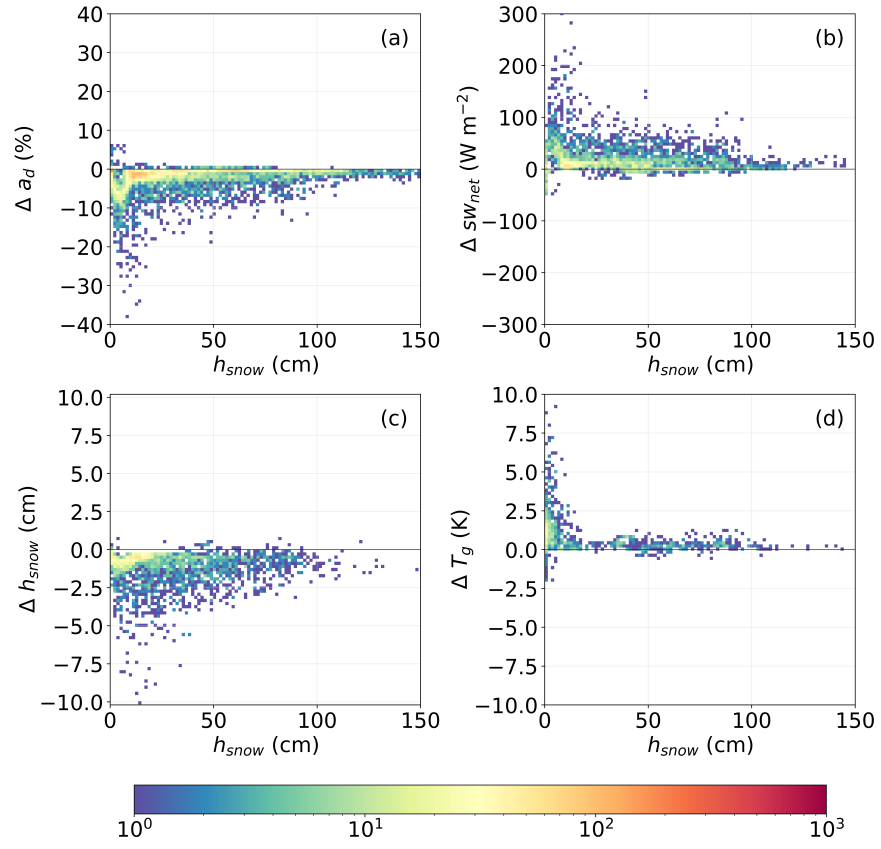












1 **Regional Impact of Snow-Darkening on Snow Pack and**  
2 **the Atmosphere During a Severe Saharan Dust**  
3 **Deposition Event in Eurasia**

4 **Anika Rohde<sup>1</sup>, Heike Vogel<sup>1</sup>, Gholam Ali Hoshyaripour<sup>1</sup>, Christoph**  
5 **Kottmeier<sup>1</sup>, Bernhard Vogel<sup>1</sup>**

6 <sup>1</sup>Institute of Meteorology and Climate Research, Karlsruhe Institute of Technology (KIT), Karlsruhe,  
7 Germany

8 **Key Points:**

- 9 • There are regional effects due to the high spatial variability in mineral dust and  
10 snow properties  
11 • Thin snow layers favor a rise in temperature, higher elevations mainly show ac-  
12 celerated snow melt  
13 • We found a significant impact on surface radiation, temperature and snow cover  
14 properties

## Abstract

Light-absorbing impurities such as mineral dust can play a major role in reducing the albedo of snow surfaces. Particularly in spring, deposited dust particles lead to increased snow melt and trigger further feedbacks at the land surface and in the atmosphere. Quantifying the extent of dust-induced variations is difficult due to the high variability in the spatial distribution of mineral dust and snow. We present an extension of a fully coupled atmospheric and land surface model system to address the impact of mineral dust on the snow albedo across Eurasia. We evaluated the short-term effects of Saharan dust in a case study. To obtain robust results, we performed an ensemble simulation followed by statistical analysis. Mountainous regions showed a strong impact of dust deposition on snow depth. We found a mean significant reduction of  $-1.4$  cm in the Caucasus Mountains after one week. However, areas with flat terrain near the snow line also showed strong effects despite lower dust concentrations. Here, the feedback to dust deposition was more pronounced as increase in surface temperature and air temperature. In the region surrounding the snow line, we found an average significant surface warming of  $0.9$  K after one week. This study shows that the impact of mineral dust deposition depends on several factors. Primarily, these are altitude, slope, snow depth, and snow cover fraction. Especially in complex terrain, it is therefore necessary to use fully coupled models to investigate the effects of mineral dust on snow pack and the atmosphere.

## 1 Introduction

Snow-covered surfaces are characterized by a high capacity to reflect solar radiation. In the visible spectrum, the albedo of pure snow is roughly 96–99% (Wiscombe & Warren, 1980). Therefore, snow surfaces play an important role in the Earth’s radiation budget. With diminishing snow cover, the landscape albedo decreases and surface warming increases. The current knowledge about the properties of snow albedo was well summarized by Skiles and Painter (2018). It is necessary to distinguish between different states of snow. Fresh snow has a very high albedo and therefore reflects almost all of the incoming solar radiation. Aged snow is less reflective, but still reflects most of the radiation. The major factors that determine the optical properties of snow are the snow microstructure, snow depth, and the content of impurities. The latter has only recently become the focus of attention.

A model for computing snow albedo with influences of light-absorbing particles was presented by Wiscombe and Warren (1980). But at first, only simplistic studies were conducted with climate models where the albedo was systematically changed (e.g., Hansen & Nazarenko, 2004; Jacobson, 2004; Hansen, 2005). This was followed by measurements (e.g., Aoki et al., 2006; Meinander et al., 2013; Peltoniemi et al., 2015; Svensson et al., 2016) and more advanced simulations involving sophisticated snow or meteorological models and aerosol properties (e.g., Flanner & Zender, 2005; Flanner et al., 2009; Dumont et al., 2014; Tuzet et al., 2017; Sarangi et al., 2019; Di Mauro et al., 2019; Tuzet et al., 2019; Donth et al., 2020; Dumont et al., 2020; Rahimi et al., 2020; Sarangi et al., 2020; Usha et al., 2020). The light-absorbing impurities (LAI) are mostly aerosols which either originate from the close surroundings or travel over long distances in the atmosphere. These aerosols can have different compositions depending on their origin.

The most frequently discussed aerosol is black carbon (BC). Due to the dark color it has the strongest impact on the snow properties (e.g., Nagorski et al., 2019; Rahimi et al., 2020; Sarangi et al., 2020). However, several studies showed that mineral dust transported to several regions (e.g., central Asia mountains, Colorado in the U.S.) outweigh BC because of its large abundance (Painter et al., 2010; Gautam et al., 2013; Kaspari et al., 2014; Yasunari et al., 2015; Svensson et al., 2018). Furthermore, Sarangi et al. (2020) demonstrated that the impact of dust can increase with altitude relative to the impact of BC. Since snow melt in high mountains often provides water supply for downstream environments and residents throughout the catchment area, the timing and amount of

67 melt water runoff is of great importance. Due to the perturbation through aerosols, this  
68 timing and amount can change significantly. Snow with aerosol contamination melts out  
69 earlier in spring time (Fujita, 2007; Painter et al., 2010; Bryant et al., 2013; Deems et  
70 al., 2013; Skiles et al., 2015). Furthermore, the aerosols on snow and ice play an impor-  
71 tant role regarding the melting of glaciers, one of the most vulnerable components of the  
72 Earth system (Xu et al., 2009; Gabbi et al., 2015; Li et al., 2017).

73 In one of the more recent studies Lau et al. (2018) used the NASA GEOS-5 (Na-  
74 tional Aeronautics and Space Administration Goddard Earth Observing System, Ver-  
75 sion 5) climate model to simulate the impact of LAI on the Eurasian continent. The im-  
76 pact of dust, BC, and organic carbon on snow cover were evaluated based on anomaly  
77 fields derived from comparing the mean climatology of 10 ensemble members, each cov-  
78 ering 10 years. They found an annual mean increase in surface skin temperature most  
79 pronounced in Western Eurasia, East Asia, and the Tibetan Plateau. In these areas the  
80 difference was greater than 2 K. The reduction in snow mass and the increase in short-  
81 wave radiation coincided with these warmed regions. There was a decrease in soil mois-  
82 ture in Western Eurasia. However, an increase was reported over India, China, and South-  
83 ern Russia.

84 Higher resolution simulations over shorter time periods were also carried out to in-  
85 vestigate the regional impact. One example is the study by Qian et al. (2009) employ-  
86 ing the WRF-Chem model (Weather Research and Forecasting - Chemistry). The fo-  
87 cus of their study was the impact of soot in a simulation of the Western United States  
88 at a grid spacing of 15 km along a year. One major finding was that about half of the  
89 decrease in landscape-scale albedo is actually caused by the changes of the snow albedo  
90 itself. The other half is attributed to the vanishing of the entire snow cover and reveal-  
91 ing the even darker surface below the snow cover. This feature is called the snow-albedo  
92 feedback and results in additional absorption of solar energy. They estimated the increase  
93 in surface shortwave net radiation flux and 2m temperature due to the soot deposition  
94  $2\text{--}12\text{ W m}^{-2}$  and  $0.2\text{--}1.4\text{ K}$ , respectively. They also noted that the spatial distribution  
95 is very heterogeneous and that the soot induced snow albedo perturbation is rather a  
96 regional effect. Therefore, greater uncertainties are to be expected with a coarser model  
97 resolution.

98 Flanner and Zender introduced the two-stream, multi-layer SNICAR (SNOW, ICe,  
99 and Aerosol Radiation) model which was thereafter used in many studies (e.g., Flanner  
100 et al., 2007, 2009, 2012; Kaspari et al., 2014; Zhao et al., 2014; Wu et al., 2018; Zhong  
101 et al., 2017; Nagorski et al., 2019; Sarangi et al., 2019). Coupled to a general circulation  
102 model, SNICAR calculates the snow albedo based on snow grain size and the theory of  
103 Wiscombe and Warren (1980) in one visible and four near-infrared bands. The optical  
104 properties of LAI were included to investigate the climate forcing of aerosols on snow  
105 (Flanner et al., 2007).

106 There are several studies that include highly sophisticated one-dimensional snow  
107 pack models like SNOWPACK (Lehning et al., 1999; Bartelt & Lehning, 2002; Lehning,  
108 Bartelt, Brown, Fierz, & Satyawali, 2002; Lehning, Bartelt, Brown, & Fierz, 2002). The  
109 snow scheme resolves multiple layers of snow and computes mass and energy exchange  
110 between the snow, the ground, and the atmosphere. Furthermore, it considers a detailed  
111 parametrization of snow metamorphism including shapes and sizes of snow grains. SNOW-  
112 PACK becomes a powerful tool when coupled with SNICAR. The coupling enables the  
113 simulation of radiative changes due to the impurities in the snow and the detailed as-  
114 sessment of the effects on the snow cover energy balance. For example, Skiles and Painter  
115 (2019) used this setup to simulate a snow cover in the San Juan Mountains in Colorado  
116 in spring to study the influence of dust on snow melt. Skiles and Painter found an av-  
117 erage daily mean radiative forcing of  $30\text{ W m}^{-2}$  which varied between 2 and  $109\text{ W m}^{-2}$ .  
118 The change in the snow albedo was quite low in the first half of the simulation with a  
119 reduction of 3% in the dust experiment. However, as soon as the melting commenced  
120 and aerosols resurfaced, the snow albedo dropped immensely resulting in a difference of  
121 44% between the two experiments. The resulting radiative forcing led to an advanced

122 snow melt by 30 days. Their study underlines the importance of a stratification of the  
123 aerosols which enables the aerosols to resurface. Moreover, the study shows the signif-  
124 icant role of aerosols in the process of snow melt in spring.

125 Similar capabilities come with the snow model Crocus (Brun et al., 1992; Vionnet  
126 et al., 2012) which incorporates TARTES (Two-stream Analytical Radiative TransfER  
127 in Snow) (Libois et al., 2013) that allows the model to simulate the radiative impact of  
128 LAI in snow. Dumont et al. (2020) used Crocus to investigate the impact of aerosols on  
129 snow melting during a major Saharan dust deposition event in the Russian Caucasus Moun-  
130 tains. The aim of the study was to capture the snow pack evolution with and without  
131 the impact of aerosols. The simulations covered the period from 1 June 2017 to 1 June  
132 2018 for several locations. Dust was deposited at a small constant rate whereas the dust  
133 event experiments had one additional deposition on 23 March 2018. They found that de-  
134 pending on dust concentration, snow layer height, and altitude, the snow melt out ad-  
135 vanced between 12–30 days. The daily averaged radiative forcing reached almost  $35 \text{ W m}^{-2}$   
136 which is in the same range as the findings of Skiles and Painter (2019). Dumont et al.  
137 (2020) pointed out that the impact is more pronounced at higher elevation due to the  
138 fact that aerosols in snow cause a stronger absorption of shortwave radiation but sensi-  
139 ble and latent heat fluxes are less impacted. The reason for this is the lower ambient  
140 temperature compared to lower elevations. In addition, Dumont et al. emphasized that  
141 the sensitivity of season shortening to dust is higher at low concentrations. However, this  
142 relationship is neither linear nor logarithmic.

143 Such sophisticated one-dimensional models like SNOWPACK and Crocus are power-  
144 ful tools that allow a precise study of the energetic processes in a snow pack. However,  
145 they do not provide information about the spatial distribution, the influence of the ter-  
146 rain, and also the feedback with the atmosphere on a larger scale. An ideal solution is  
147 coupling a complex snow model with an earth system model, but this is not possible at  
148 least operationally due to the immensely high computational costs. Global models are  
149 therefore relying on more simplified snow models that give less information about the  
150 internal structures of the snow layer but allow a bit more insight into the interaction of  
151 other earth system components in return.

152 The study of Rahimi et al. (2020) is one example how such a model framework can  
153 be utilized to study the radiative impact of aerosols on snow. The base of their inves-  
154 tigation was the WRF-Chem model in a convection-resolving grid (4 km) coupled with  
155 SNICAR. Their study area was the Rocky Mountains in the United States. Rahimi et  
156 al. (2020) found that both, mineral dust and BC have a positive radiative impact when  
157 deposited on snow surfaces. Dominant in this manner was BC with a positive radiative  
158 forcing of more than  $2 \text{ W m}^{-2}$ . The positive radiative forcing of aerosols in snow super-  
159 imposed a slightly negative radiative forcing of aerosols in the atmosphere. This conclu-  
160 sion was also supported by a study by (Usha et al., 2020). Furthermore, Rahimi et al.  
161 found a general increase in 2m temperature by 0.15 K and an earlier snow melt out of  
162 4 days. In this study, they found a 2% reduction in snow albedo at high altitudes and  
163 an increased snow grain size by several microns due to the aerosols in snow. At some lo-  
164 cations an increase in snow water equivalent was evident despite reduced snow albedo.  
165 They suggest that an increase in snow water equivalent or a decrease in temperature de-  
166 spite the positive radiative forcing of aerosols is caused by internal model variability. They  
167 argued that due to limited computational resources, it was not possible for them to fur-  
168 ther investigate the internal model variability.

169 We extended the model system ICON-ART (ICOsahedral Nonhydrostatic atmo-  
170 sphere and climate with Aerosols and Reactive Trace gases) by a parametrization of a  
171 spectral snow albedo which considers snow aging processes and the darkening effect of  
172 mineral dust on snow in 18 wavelength bands. As a result, we obtained a framework fea-  
173 turing an atmospheric and land model system, that allows the online computation of the  
174 impact of mineral dust on snow and the associated feedback of the land surface and the  
175 atmosphere. For the first time, the effects of mineral dust on snow have been simulated

176 with high spectral resolution in an extensive ensemble simulation setup. This setup al-  
177 lows statistically robust results on short-term effects of mineral dust on snow.

178 The impact of Saharan dust was investigated in a simulation covering Europe and  
179 western parts of Asia. In spring 2018 a particularly impactful dust event occurred (Solomos  
180 et al., 2018; Marmureanu et al., 2019; Barkan & Alpert, 2020; Dumont et al., 2020; Mon-  
181 teiro et al., 2022). We investigated this event with the fully coupled model system ICON-  
182 ART to disentangle regional influences and drivers on the snow-darkening effect. The  
183 goal was to assess the spatial and temporal distribution of the mineral dust during this  
184 event and to quantify the resulting feedback. The questions that we addressed in this  
185 study are: 1) does the distribution of mineral dust result in the formation of particularly  
186 vulnerable regions? 2) how intense can the feedbacks in the land surface and the atmo-  
187 sphere be during the severe dust event? 3) which surface and atmospheric variables are  
188 most strongly affected during this event. The paper is organized as follows: in section  
189 2 we explain the methodology and assumption which is followed by the results and dis-  
190 cussions in section 3. We summarize the results and provide the conclusions in section  
191 4.

## 192 2 Methodology

### 193 2.1 ICON-ART Model System

194 The ICON model is a weather and climate model that solves the full three-dimensional  
195 non-hydrostatic and compressible Navier-Stokes equations (Zängl et al., 2015; Giorgetta  
196 et al., 2018). The equations are discretized on an unstructured triangular grid that is  
197 based on a spherical icosahedron. This feature allows the model to operate at various  
198 scales and be refined seamlessly. The results of a global simulation run can be used to  
199 drive an ICON simulation in the regional configuration LAM (Limited Area Mode). In  
200 this study, the radiation in ICON is treated by the RRTM (Rapid Radiative Transfer  
201 Model) described by Mlawer et al. (1997). This radiative transfer model calculates short-  
202 wave and longwave radiation in 30 spectral bands between 0.2–1000  $\mu\text{m}$ .

203 At the lower boundary of the atmosphere, ICON is coupled with the land surface  
204 and vegetation model TERRA\_ML. The land surface model serves as a transmitter of  
205 heat, moisture, and momentum between the atmospheric component and the land sur-  
206 face (Doms et al., 2018). Interactions include, for example, surface roughness length, vegetation-  
207 dependent evaporation, vertical heat, water transport in the soil, photosynthetic active  
208 radiation, surface albedo, and snow cover. TERRA\_ML provides two different snow mod-  
209 els. The first is used in operational weather forecast and is a single-layer snow model.  
210 As pointed out by previous studies (e.g., Jacobi et al., 2015) a single-layer snow model  
211 scheme is not capable to adequately represent the energy budget and the temperature  
212 profile in a snow pack. Usually, the snow layer tends to disappear too early in spring-  
213 time in such models. Furthermore, the ability to create an aerosol stratification, which  
214 describes the vertical distribution of the aerosols in snow, is not possible when having  
215 only one single layer. As pointed out by Skiles and Painter (2019), the resurfacing of the  
216 aerosols plays a major role in the optical properties of the snow. These are the main as-  
217 pects why in this study an experimental snow model is used that was developed at Ger-  
218 man weather service (DWD) (Machulskaya & Lykosov, 2008). It is also incorporated in  
219 the TERRA\_ML surface scheme with adjustable number of snow layers. The applica-  
220 tion of multiple snow layers allows for vertical profiles of snow temperature, water con-  
221 tent, and snow density.

222 ART is a sub-module of ICON that enables the simulation of aerosols, trace gases,  
223 and related feedbacks (Rieger et al., 2015; Schröter et al., 2018). It can treat various aerosol  
224 types including sea salt, volcanic ash, mineral dust, and several gaseous tracers. The DWD  
225 provides ICON-ART mineral dust forecasts, which are available for comparison with re-  
226 sults from other forecasting systems on the SDS-D-WAS (Sand and Dust Storm Warn-  
227 ing Advisory and Assessment System) home page (<https://sds-was.aemet.es/forecast>)

228 -products/dust-forecasts/forecast-comparison, last access December 9, 2022). A  
229 detailed description of the treatment of aerosol processes can be found in Rieger et al.  
230 (2015); Schröter et al. (2018). In this work, we use the two-moment aerosol description.  
231 The mineral dust is represented in three log-normal modes. The optical properties of dust  
232 in ART are extinction coefficient, single-scattering albedo, and asymmetry parameter  
233 (Rieger et al., 2017; Gasch et al., 2017). The dust emission is calculated online and based  
234 on soil type, soil moisture content and wind speed. The parametrization is based on Vogel  
235 et al. (2006) and accounts for emission due to saltation. Mineral dust can leave the at-  
236 mosphere via sedimentation, dry, and wet deposition. When the aerosols are removed  
237 from the atmosphere, they reach the land surface. We add these aerosols to the snow  
238 cover, if such is present. The particles are finally removed from the system as soon as  
239 the snow cover disappears.

## 240 2.2 Dust and Snow Interaction

241 We introduced a new prognostic variable, the optical equivalent snow grain radius,  
242 into the experimental snow model. Furthermore, we incorporated a parameterization for  
243 the growth of the snow grains. This aging process is based on the equation of Essery et  
244 al. (2001). However, we extended the aging factors for additional temperature ranges (Jäkel  
245 et al., 2021) and added the influence of rain. The snow grain size constitutes the basis  
246 for the computation of the spectral snow albedo. For this purpose, we incorporated the  
247 theory of Wiscombe and Warren (1980) into the model. It is based on the Mie theory  
248 (Mie, 1908) which describes the scatter properties of spherical particles. We used the nec-  
249 essary refractive indices from the collection of Warren and Brandt (2008). A detailed de-  
250 scription of our developments are available in Rohde (2021).

251 We incorporated the interaction of the optical properties of mineral dust and snow  
252 at the top of the snow pack, adjoining the atmosphere. This interaction happens in the  
253 model from the top to a defined snow depth which was fixed to 10 cm, in this study. Ac-  
254 cording to Warren and Wiscombe (1980), the modification of the snow albedo due to aerosols  
255 is carried out by weighted averaging of the extinction cross sections and scatter cross sec-  
256 tions using the total cross sections as weighing factors. The interaction is computed on-  
257 line in 18 wavelength bands ranging from 0.30–1.65  $\mu\text{m}$ . Our computations assume an  
258 external mixing of snow and mineral dust. It needs to be pointed out that the external  
259 mixing is mostly apparent when dust deposits under dry conditions. In the case of wet  
260 deposition, internal mixing occurs. A couple of studies investigated the snow-darkening  
261 effect of internally mixed aerosols in snow and found out that the darkening is further  
262 enhanced due to internal mixing (Flanner et al., 2012; Shi et al., 2021).

263 We assume that dust particles remain in the snow layer where they are deposited  
264 to. We introduced tracking of mineral dust by linking the dust mass to the height of the  
265 respective snow layer above the ground. We consider the mineral dust mass to be uni-  
266 formly distributed within a snow layer. A shifting of the position of the aerosols is only  
267 taking place when the total snow depth changes. Regarding this, snowfall, compression  
268 and other physical processes are ignored in this approach. We assume that both snow  
269 melt and accumulation of snow occur at the upper boundary toward the atmosphere. Fig-  
270 ure 1 illustrates the transfer of dust mass between snow layers during snow accumula-  
271 tion and snow melt.

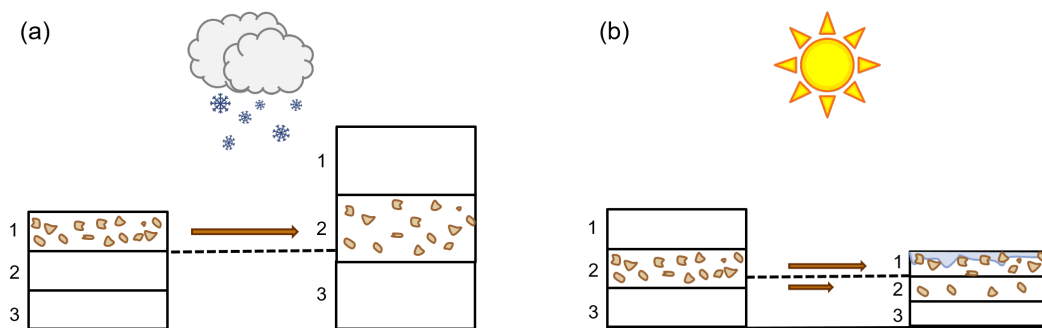


**Figure 1.** Conceptual diagram of aerosol mass transfer between snow layers during (a) snow accumulation and (b) snow melt.

### 2.3 Model Configuration

We performed a global simulation of a dust event at a horizontal resolution of about 40 km (R2B06). The simulation covered the time period of March 22, 2018, 0 UTC to April 1, 2018, 0 UTC (10 days). At start of the simulation, the model was initialized using two different sources. The meteorological state was initialized using ECMWF - IFS (European Centre for Medium-Range Weather Forecasts - Integrated Forecasting System) data from March 22, 2018, 0 UTC. The mineral dust data were obtained from the operational dust forecast using ICON-ART performed by the DWD.

The simulation was a free run without reinitialization throughout the 10 days. Due to the fact that both the deposition and the snow cover are strongly dependent on the terrain and that they are spatially highly variable, the resolution of 40 km was further increased. For this purpose, we applied the ICON-ART LAM with the horizontal resolution of 10 km (R2B08) during the same time period. The hourly results of the meteorological variables as well as the mineral dust of the global R2B06 simulation were used to force the LAM domain. The investigation area extends over large parts of the snow-covered areas of Europe and Asia between  $30^{\circ}$ – $70^{\circ}$  N and  $10^{\circ}$  W– $70^{\circ}$  E.

Figure 2 shows the study region of the ICON-ART LAM domain and the two smaller regions where certain processes are investigated in more detail. Region A covers the Caucasus Mountains, where a severe dust deposition event was reported (Barkan & Alpert, 2020; Dumont et al., 2020). It covers the area between  $40.5^{\circ}$ – $45^{\circ}$  N and  $39^{\circ}$ – $49^{\circ}$  E. Region B covers the snow line which moves towards the north due to spring melting processes. Here, the term does not refer to the snow line which indicates the lower limit of the snow cap at high terrain. Instead, the term 'snow line' refers to the ever-changing equatorward limit of the snow cover. This snow line migrates due to seasonal changes. In cold seasons, this boundary lies further south, and in warm seasons, it lies in northerly territories. Region B extends over the area between  $45^{\circ}$ – $53^{\circ}$  N and  $22^{\circ}$ – $70^{\circ}$  E. The ongoing melting during springtime makes the snow especially receptive for the influence of aerosol particles (Skiles & Painter, 2019). According to Lau et al. (2018), this is one of the main vulnerable regions to aerosol deposition on the Eurasian continent.

To investigate the influence of mineral dust on snow surfaces, two sets of experiments were executed in parallel. The reference experiment (REF) contains all new implementations concerning the spectral snow albedo, but excludes the interaction of the optical properties of mineral dust and snow. In other words, the mineral dust is present in the reference experiment but does not affect the snow albedo. It is assumed that the snow is clean. We performed a second experiment with the same set up as the reference experiment but the interaction of the optical properties of dust and snow is included. This corresponds to the snow-darkening simulation (SDS).

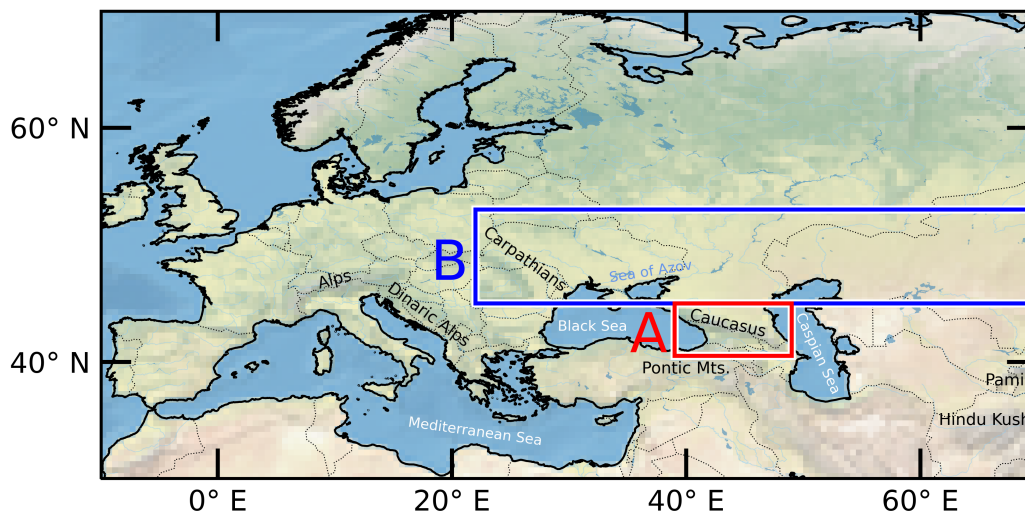


**Figure 2.** ICON-ART LAM domain with outlines of region A including the Caucasus Mountains and region B containing the moving snow line during spring time melt in March 2018.

309 Rahimi et al. (2020) highlighted that a large variability prevails at higher resolu-  
 310 tion caused by internal model variability. To achieve a more robust result, we performed  
 311 ensemble simulations. The application of ensemble simulations is a well established method  
 312 for the identification of result uncertainties. This tool is used in particular in numeri-  
 313 cal weather prediction, where short time periods are computed at high resolution. For  
 314 the analysis, we consider the arithmetic mean over all individual simulation results. We  
 315 generated the members via a stochastic perturbation of model internal physical param-  
 316 eters within their uncertainty range. The same perturbation was introduced pairwise in  
 317 one REF and one SDS simulation which allows for a comparison of the experiments. In  
 318 this way, 40 pairs were generated and a total of 80 simulations. The influence of min-  
 319 eral dust is determined by the arithmetic mean over all individual differences between  
 320 the respective simulation pairs (SDS–REF). All variables refer only to cells in which at  
 321 least one ensemble member, either SDS or REF, contains snow. Other cells that are com-  
 322 pletely snow free in all ensemble members were excluded from the analysis. To investi-  
 323 gate the local and instantaneous effects, and to obtain a high confidence that the effects  
 324 can actually be attributed to the aerosol deposition on snow, we performed a significance  
 325 analysis.

326 The significance analysis focused on the significance of individual cells in the con-  
 327 text of all paired simulations. We applied the Wilcoxon signed-rank test (Wilcoxon, 1945),  
 328 testing each cell of the 40 ensemble members including the aerosol-snow-albedo inter-  
 329 action (SDS) against the 40 members without the interaction (REF). The test evaluates  
 330 whether the two samples originate from the same distribution and returns a  $p$ -value which  
 331 describes the probability of obtaining these results if the two sets originate from the same  
 332 distribution. In most studies, all values where  $p < 0.05$  are declared as significant re-  
 333 sults and  $p < 0.01$  as highly significant results. This ‘naive-stippling’ approach leads  
 334 to many false detection of seemingly significant cells (Wilks, 2016). To minimize the false  
 335 discovery rate (FDR), we applied the approach of Wilks (2016). In contrast to the stip-  
 336 pling method, where the condition for significance is fixed to a constant  $p$ -value, this method  
 337 uses a variable threshold dependent on sample size. The control level  $\alpha_{\text{FDR}}$  was 0.2 in  
 338 this study.

## 2.4 Total Attenuated Backscatter from CALIOP

In order to verify the predicted transport of mineral dust, we compared the attenuated backscatter of the simulated mineral dust with measurements from the CALIOP (Cloud-Aerosol Lidar with Orthogonal Polarization) instrument. The instrument is a two-wavelength polarization-sensitive lidar with three receiver channels. CALIOP measures in one channel the 1064 nm backscatter intensity and in two channels the orthogonally polarized components of the 532 nm backscatter signal. It was designed to obtain high-resolution vertical profiles of aerosols and clouds (D. Winker et al., 2004; D. M. Winker et al., 2007). The CALIOP lidar is on board the CALIPSO satellite (Cloud-Aerosol Lidar and Infrared Pathfinder Satellite Observations). We use CALIOP Level 1 version 4.1 total attenuated backscatter at 532 nm of two measurements for validation. The first measurement was conducted on March 22, 2018, with the satellite overflying both dust source area and study region. The second observational data we considered was acquired on March 23, 2018 and includes a cross section of the study area. ICON-ART comes with a forward operator for attenuated backscatter at 355 nm, 532 nm and 1064 nm that enables direct comparison of the model results with CALIOP measurements (Hoshyaripour et al., 2019). We fitted the data to the corresponding resolution of the simulation by horizontal averaging. This means that, on the one hand, we brought the initial measurement data to a horizontal resolution of about 40 km. We compared these data with the results of the global simulation, which includes the dust source area. We brought the second set of measurement data to a horizontal resolution of about 10 km. This data on the other hand was compared with the results of the LAM simulation.

## 3 Results and Discussion

In this section, we present the results in four parts. First, we show a brief comparison of the atmospheric mineral dust between simulation and remote sensing data. Then, we present the temporal evolution of the mineral dust event in the study areas A and B. This is followed by the analysis of the horizontal distribution at the time of the strongest impact of mineral dust. In the last section, we discuss the feedbacks and the regional dependencies in detail.

### 3.1 Validation With CALIOP Measurements

During the transport of the mineral dust in the March 2018 event, the mineral dust was well visible in various satellite images. However, the dust was largely accompanied by thick clouds. These clouds constitute a limitation for many satellite algorithms. In this case, the aerosol optical thickness observations were not suitable for model validation. Instead, we considered measurements of the total attenuated backscatter observed by the CALIOP instrument. Cloud-free regions are included in these data, from which we can draw information about the location as well as the vertical structure of the mineral dust plume. We validated our results with two individual measurements. Figure 3 shows a comparison of total attenuated backscatter measurements at 532 nm from the CALIOP instrument and the corresponding simulated attenuated backscatter of mineral dust at two different states.

Figure 3(a) shows the measurement on 22 March, 00:18 UTC. These observational data include the backscatter of all constituents in the atmosphere including clouds. Thick clouds are characterized by particularly high attenuated backscatter. This extends to the point where the signal is attenuated in such manner that a measurement as far as the earth's surface is no longer possible. Such situations with strongly attenuated backscatter in great altitude appear in figure 3(a). They are visible as red to gray patches with dark blue shadows. The region between 14° and 31° latitude, indicated by the white dashed lines, remains largely free of such limitations. The respective simulation result is shown below in Figure 3(b). It shows the mineral dust attenuated backscatter at 532 nm of the

389 global ICON-ART simulation one hour after initialization (22 March 01:00 UTC). Solely  
390 the attenuated backscatter of mineral dust is shown here and not that of other compo-  
391 nents, such as clouds. Therefore, we focus initially on the area between  $14^\circ$  and  $31^\circ$  lat-  
392 itude. The horizontal as well as vertical structure of the attenuated backscatter between  
393 both figures are comparable. This region includes the northeastern part of the Sahara  
394 and thus the source area of the mineral dust. Although the structure between simula-  
395 tion and measurement are comparable, there is a slight difference in the intensity of the  
396 attenuated backscatter. The simulation results show a higher backscatter at ground level  
397 and a weakening of the signal up to about 4 km height. The CALIOP measurements indi-  
398 cate a rather constant backscatter intensity up to an altitude of 5 km. There may be  
399 several reasons for this discrepancy. For example, there could be variations in the size  
400 distribution of the mineral dust particles at emission. In this case, this could result in  
401 different vertical distributions due to different lifting and sinking processes. Figure 3(b)  
402 shows that the dust plume continues north of  $31^\circ$  latitude towards Europe reaching an  
403 altitude of 10 km in our simulation. Unfortunately, this cannot be directly traced in the  
404 observational data due to the limitations discussed above. However, it is remarkable that  
405 the supposedly observed cloud top north of  $31^\circ$  has a similar structure as the top of the  
406 simulated dust plume. Since the horizontal and vertical extent of the mineral dust plume  
407 in the cloud-free region (white dashed lines) agree well, it can be assumed that this is  
408 also the case north of  $31^\circ$ . Thus, we assume that the mineral dust is embedded under  
409 and in the clouds.

410 The two figures below (c and d) show the attenuated backscatter at a later time  
411 along another CALIPSO flight track. Figure 3(c) shows the CALIOP measurements on  
412 23 March at 10:03 UTC. This observation is also characterized by large areas with strongly  
413 attenuated backscatter at high altitudes, most likely due to clouds. An area at approx-  
414 imately  $35^\circ$  and  $40^\circ$  latitude is marked (white dashed lines), where such high attenuated  
415 backscatter does not occur. Here, the increased backscatter is most likely caused by the  
416 Saharan dust particles. Increased attenuated backscatter is detected at about 3 to 8 km  
417 altitude. Furthermore, there is increased attenuated backscatter preceding the moun-  
418 tains at  $35^\circ$  latitude, reaching even to ground level. Figure 3d shows the results of the  
419 LAM-simulation on 23 March at 10:00 UTC. In the region between  $35^\circ$  and  $40^\circ$  latitude  
420 the simulated attenuated backscatter of mineral dust shows a similar pattern as the to-  
421 tal attenuated backscatter observed by the CALIOP instrument. The dust plume ex-  
422 tends to an altitude of about 8 km and is visible at ground level at about  $35^\circ$  latitude.  
423 Near the ground, the simulated attenuated backscatter is slightly stronger compared to  
424 the observation. Due to the proximity to further sources, deviations in the emission pa-  
425 rameters, such as size distribution, might have an influence on the deviation of backscat-  
426 ter intensity. The simulation results show, north of  $40^\circ$  latitude, the dust plume prop-  
427 agates and reaches  $50^\circ$  latitude. Unfortunately, again we cannot draw a direct compar-  
428 ison in the observational data due to constraints. However, it is again clearly visible that  
429 the upper boundary of the signal in the CALIOP data, which is presumably caused by  
430 clouds, corresponds to the pattern of the upper boundary of the simulated dust plume.  
431 We conclude that the mineral dust is located inside and below the clouds. Due to the  
432 similar patterns and the agreement between  $35^\circ$  and  $40^\circ$  latitude the simulation results  
433 appear plausible. At approximately  $41^\circ$  latitude, the simulated dust plume reaches the  
434 ground level. In this region, close to the Caucasus Mountains, we can identify the dust  
435 deposition in the simulation results (Figure 3(b)). Figure 3(e) shows the two overflight  
436 paths of CALIPSO and the lidar measurements corresponding to figures (a) and (b) in  
437 pink and (c) and (d) in green.

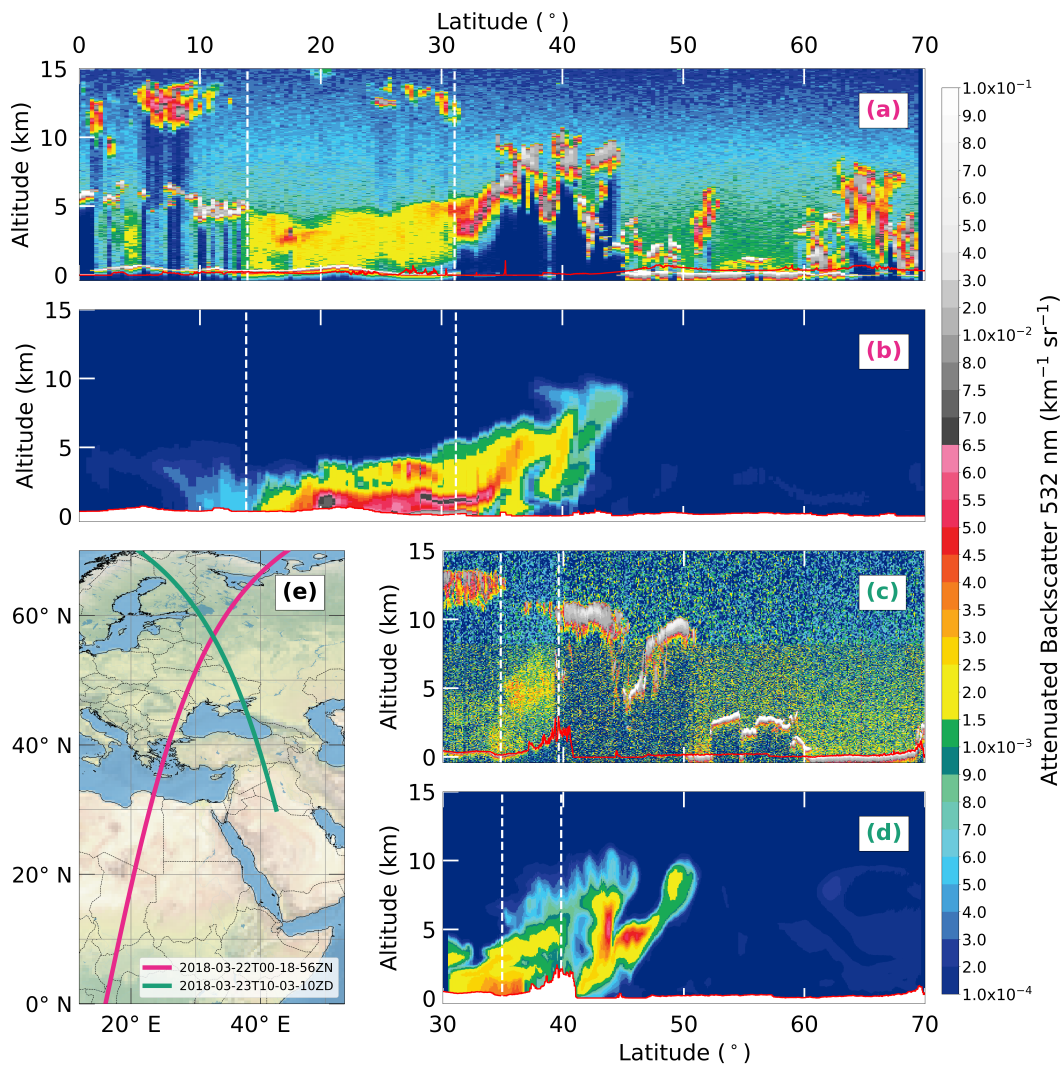


**Figure 3.** The CALIOP total attenuated backscatter for 532 nm between 0° and 70° latitude on 22 March 2018 at around 00:18 UTC (a), the corresponding dust attenuated backscatter for 532 nm of the ICON-ART global simulation at 01:00 UTC (b), the CALIOP total attenuated backscatter for 532 nm between 30° and 70° latitude on 23 March 2018 at around 10:03 UTC (c), the corresponding dust attenuated backscatter for 532 nm of the ICON-ART LAM model result at 10:00 UTC (d), and the CALIPSO ground track on 22 March 2018 at 00:18 UTC in pink and on 23 March 2018 10:03 UTC in green (e).

### 3.2 Temporal Evolution in Region A and B

The course of the Saharan dust event was summarized by (Barkan & Alpert, 2020). A cold front extended from Scandinavia to Western Sahara. This caused a severe dust storm that lifted huge amounts of Saharan dust in the air. Southwesterly flows transported the mineral dust particles within two days to Eastern Europe. In the morning of March 23, 2018, the dust deposited together with snow. The chemical composition of samples taken on March 24 near Bucharest, Romania, indicated the Northern Sahara as the dust source (Marmureanu et al., 2019). Figure 4 shows the simulated temporal evolution of mineral dust mass in the top snow layer (a), the differences between SDS and REF in diffuse surface albedo (b), surface shortwave net radiation flux (c), snow depth (d), surface temperature (e) and 2m temperature (f). These are results of the study region A extending over the Caucasus Mountains (red) and region B focusing on the extended area containing the snow line (blue). Depicted are the spatially averaged hourly results.

Wet deposition of mineral dust was observed in the Caucasus region (Sochi) in the morning of March 23, 2018. The transport of Saharan dust ceased on March 24 to March 25 but strengthened again on March 26 to March 27 (Barkan & Alpert, 2020). Our results indicate the increase in the mean mineral dust mass in the top snow layer also from March 23 on. The mean dust loading in region A reaches the first maximum of  $0.6 \text{ g m}^{-2}$  on March 24, 13 UTC. After that, dust free precipitation reduced the average dust loading in the top snow layer. As reported by Barkan and Alpert (2020), further Saharan dust transport occurred from March 26. The simulated daily mean dust loading over the whole region A reaches a maximum on March 29 at 9 UTC ( $0.9 \text{ g m}^{-2}$ ). Thereafter, the mean dust concentration drops rapidly as the dust was covered anew by dust free snowfall.

The difference between SDS and REF in surface albedo develops with the accumulation of mineral dust in region A. A first maximum in the reduction in surface albedo is reached on March 24, 14 UTC. The reduction in surface albedo due to mineral dust is at that point  $-1.2\%$ . In the later stages, the surface albedo experiences even greater reductions. On March 28, 9 UTC and March 29, 9 UTC further maxima are reached with a decrease ranging up to  $-1.7\%$  and  $-1.4\%$ , respectively. The overall mean reduction in surface albedo during sunlit hours in region A is  $-0.7\%$ . The largest daily reduction in surface albedo occurs on March 28, with an averaged difference of  $-1.4\%$ .

The increase in surface shortwave net radiation flux grows from day to day with the decrease in surface albedo. The influence is strongest at the peak of sun elevation. However, the occurrence of the phenomenon depends on the prevailing conditions. For example, the radiative effect at the surface can be negative despite the reduced surface albedo. This happens when the cloud cover or the precipitation differs in the two experiments. This is the case after March 29. The shortwave net radiation flux shows that both experiments diverge in the atmospheric conditions. Therefore, we focus on March 29 for the more detailed spatial analysis. On March 29, the daily maximum in region A reaches a difference of  $8.0 \text{ W m}^{-2}$ . However, the overall maximum is already reached on March 28 with a difference of  $10.2 \text{ W m}^{-2}$ .

Figure 4d shows that the difference in snow depth between the two experiments increases during daytime. Throughout the dust event, the difference in region A continues to grow until March 29. At this point the maximum difference of  $-0.5 \text{ cm}$  is reached. Due to fresh snowfall without mineral dust, the difference decreases again after this day.

The differences between SDS and REF in surface temperature and 2m temperature indicate that the relationship with mineral dust deposition is somewhat more complicated than the relationship between surface albedo or surface shortwave net radiation flux with dust accumulation. There are many fluctuations, but mainly warming occurs in the SDS experiment. Similar to the previous variables, the largest differences occur around midday. The strongest increase in the two variables is reached on the last two days. Here, however, it is uncertain whether this warming was induced directly by the mineral dust deposition. Opposed to this is the fact that the difference in shortwave radiation absorption is only moderate. If we exclude the last two days, the largest temperature increase occurs on March 29. Here the increase in surface temperature and 2m tem-

493 perature reaches an extend of 0.09 K and 0.05 K, respectively. That means on average  
494 the temperature changes in the lowest layer of the atmosphere are quite small.

495 Region B was less affected by the Saharan dust event and shows less variability in  
496 the temporal analysis. The accumulation of mineral dust in the top snow layer gradu-  
497 ally increases and reaches a maximum value of  $0.15 \text{ g m}^{-2}$  on the last simulation day. The  
498 mean difference in surface albedo between the two experiments increases with each pass-  
499 ing day. The albedo reduction due to Saharan dust averaged over the course of the day  
500 is largest on March 30 and reaches  $-0.9\%$  in region B. The largest radiative forcing oc-  
501 curs on the last three simulation days. At the daily maximum an additional surface short-  
502 wave net radiation flux of  $3.3 \text{ W m}^{-2}$ ,  $3.8 \text{ W m}^{-2}$ , and  $3.1 \text{ W m}^{-2}$  occurs on March 29,  
503 30, and 31, respectively. The strongest decrease in snow depth happens in region B on  
504 March 30, with a difference of  $-0.2 \text{ cm}$ . High variability in the differences in surface tem-  
505 perature and 2m temperature are also evident in this region. The difference in surface  
506 temperature ranges between  $-0.04$  and  $0.09 \text{ K}$  over the entire period. However, there is  
507 a warming of the surface for 89% of the simulated time span. The difference in 2m tem-  
508 perature varies between  $-0.04 \text{ K}$  and  $0.06 \text{ K}$ . We found no significant effect on cloud cover  
509 or precipitation in the temporal analysis in either region A or B (not shown).

510 It is apparent that the formation of feedback in the different variables requires a  
511 certain leading time. The largest differences between SDS and REF appear in region B  
512 on the last day, indicating that the repercussions have not reached a threshold within  
513 the simulated 10 days and possibly may even expand. This depends on the development  
514 of the weather conditions. An important aspect to consider here is that the snow in our  
515 simulation is completely aerosol free at the initial stage. This could lead to an under-  
516 estimation of the dust loading in snow, since background concentration that accumulated  
517 before the major dust event are not captured. Dumont et al. (2020) reported that the  
518 dust deposition was covered by clean snow after a few days in the Caucasus. We found  
519 the same in our simulation results. With large amounts of new snow, the effect of min-  
520 eral dust on snow can be quickly removed. However, Dumont et al. (2020) stated that  
521 with snow melting after a few weeks, the aerosols were again exposed and concentrated  
522 at the snow surface. As a result, the deposited mineral dust again had an impact on snow  
523 melt. This means that the effects of an extreme dust deposition event are not only of  
524 short duration but can have far-reaching consequences for the snow cover during the whole  
525 season. We found the strongest feedbacks in almost all variables around midday. An ex-  
526 ception is the snow depth. Here the greatest reduction is shifted to the end of the day.

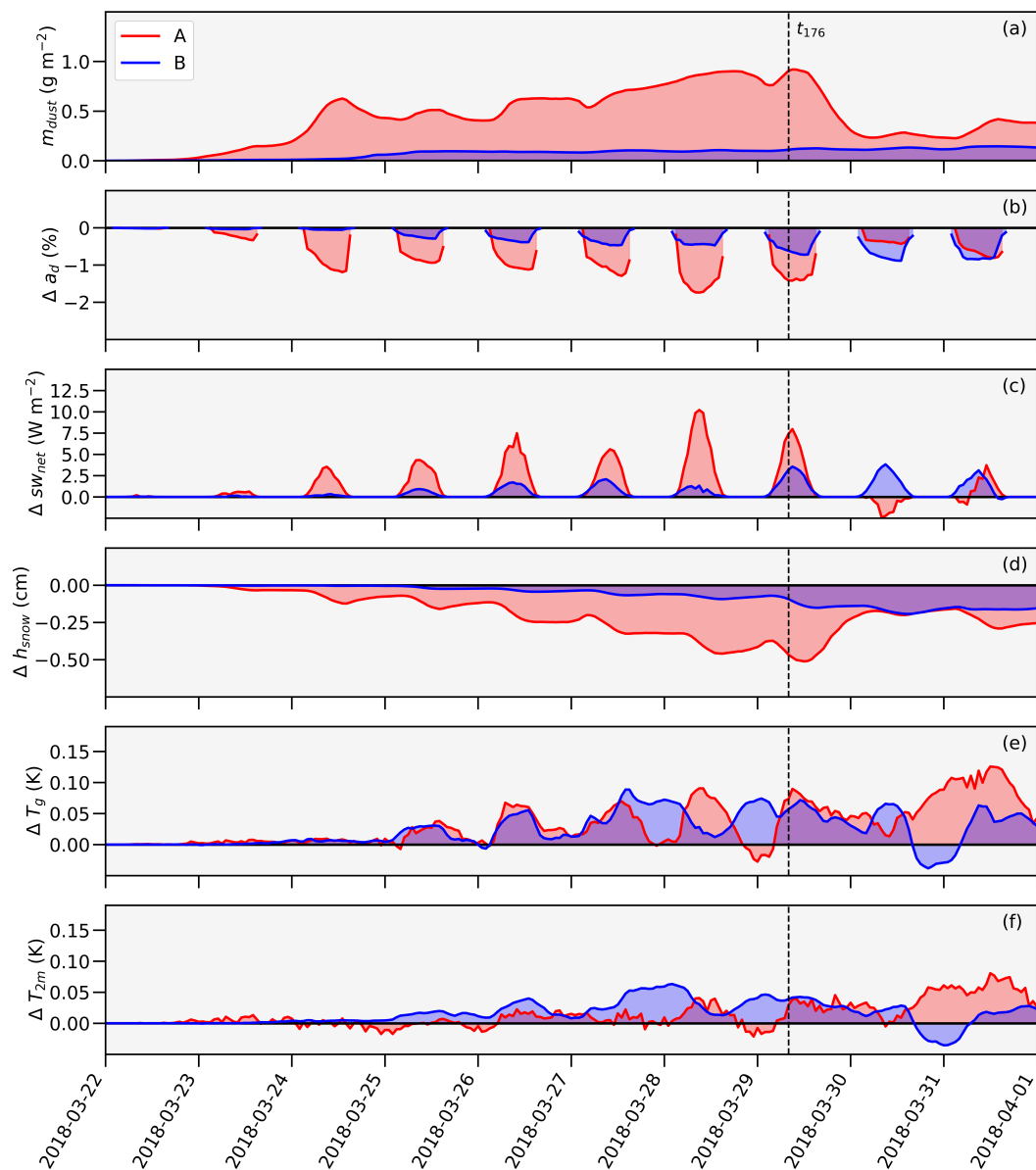


**Figure 4.** Spatially averaged hourly simulation results of mineral dust deposition in the top snow layer (a), the differences (SDS–REF) in surface albedo (b), surface shortwave net radiation flux (c), snow depth (d), surface temperature (e), and 2m temperature (f) across region A (red) and B (blue).

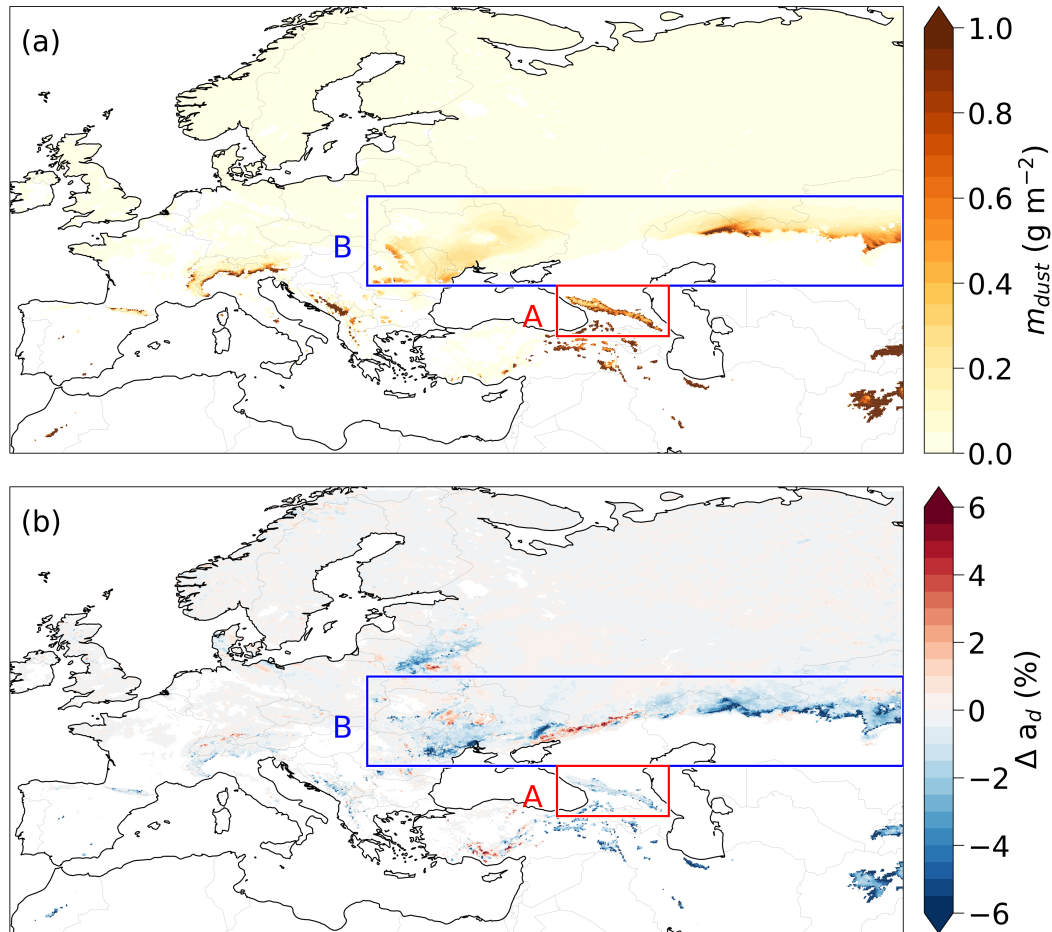
### 3.3 Spatial Distribution

Figure 5 shows the ensemble mean distribution of mineral dust in the top snow layer in SDS (a) and the ensemble mean difference in diffuse surface albedo between SDS and REF on snow-covered surfaces (b) on March 29, 8 UTC, after 176 hours of simulation ( $t_{176}$ ). Mineral dust accumulates mainly on mountain ranges. This is clearly visible on the south-facing slopes of the Pyrenees, the Alps, the Dinaric Mountains, and the Carpathians. In addition, the Caucasus Mountains and parts of the Pontic Mountains adjacent to them in the south have high levels of mineral dust in snow. In the southeast of the model domain, parts of the Hindu Kush and the Pamirs are identifiable. They show a higher influence by mineral dust, but they are not in the focus of this study. Surprisingly, higher levels of mineral dust are present along the snow line in Kazakhstan, although the terrain is rather flat. This is connected to higher surface concentration due to the successive melting back of the snow line. The mean dust loading of the whole model domain at  $t_{176}$  is  $0.1 \text{ g m}^{-2}$  with a local maximum of  $32.9 \text{ g m}^{-2}$  (Baba Mountain range, western extension of the Hindu Kush). Region A has a mean dust loading of  $0.9 \text{ g m}^{-2}$  and a local maximum of  $11.7 \text{ g m}^{-2}$  at this point. Region B has a mean dust loading of  $0.1 \text{ g m}^{-2}$  and a local maximum of  $1.7 \text{ g m}^{-2}$ .

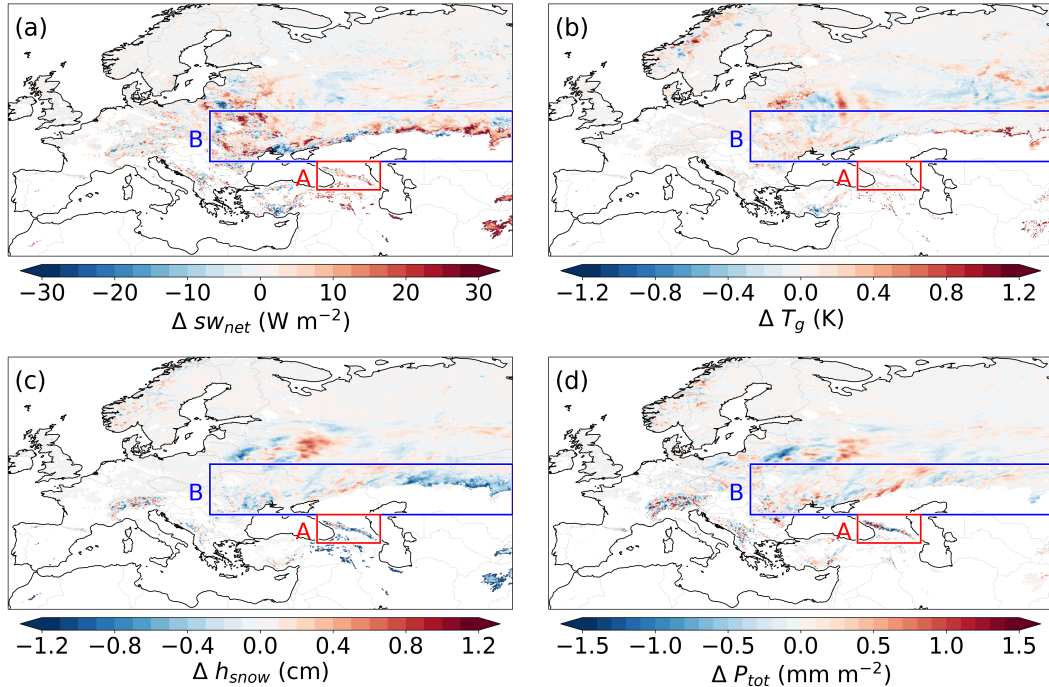
The patterns of ensemble mean difference in diffuse snow albedo between SDS and REF shows similarities to the mineral dust distribution (Figure 5b). The largest differences in surface albedo between the two experiments are mainly apparent at places with higher dust concentration. Thus, complex terrain is strongly affected by a reduction in surface albedo. The areas along the snow line also show a strong reduction except for an area in Russia northeast of the Black Sea. The area of the Caucasus Mountains shows a particularly clear negative signal in diffuse surface albedo as well. Furthermore, areas in the northwestern corner of the Black Sea as well as some areas in Belarus are characterized by reduced surface albedo in SDS. The ensemble mean reduction in surface albedo in SDS is  $-0.4\%$  over the whole area,  $-1.4\%$  in region A and  $-0.6\%$  in region B. The respective standard deviations are  $1.2\%$ ,  $1.5\%$  in region A and  $1.5\%$  in region B. The values of the strongest reduction in these areas are correspondingly  $-38.4\%$ ,  $-13.4\%$ , and  $-16.0\%$ .

Figure 6 shows the ensemble mean difference patterns of surface shortwave net radiation flux (a), surface temperature (b), snow depth (c), and total precipitation (d) between SDS and REF on snow-covered surfaces on March 29, 8 UTC, after 176 hours of simulation ( $t_{176}$ ). The signal in surface shortwave net radiation flux appears relatively chaotic. There are several areas where an increase in the radiation flux appears, but there are also areas where the radiation flux decreases. This is mainly due to the pattern of the cloud cover. A slight shift of the location of the clouds results already in strong signals. Particularly in Eastern Europe, a noisy pattern is evident that is not related to mineral dust deposition or changes in surface albedo. The surfaces in the Caucasus Mountains as well as in areas near the snow line are characterized by a strong increase in shortwave radiation flux. An exception is an area northeast of the Black Sea, where a decline occurs. There is a clear positive radiative forcing when considering spatial averages. At  $t_{176}$  the difference between SDS and REF is  $1.5 \text{ W m}^{-2}$  in the whole study region,  $7.4 \text{ W m}^{-2}$  in region A and  $3.2 \text{ W m}^{-2}$  in region B.

The difference in surface temperature between the two experiments is illustrated in Figure 6b. A strong increase in surface temperature due to mineral dust deposition is almost exclusively evident along the snow line. Northeast of the Black Sea, the surface temperature in SDS is in turn lower. The increased surface albedo also occurs at this location (Figure 5b). But there are differences, especially on the Russian territory, that cannot be attributed to the changes in albedo and do not exactly match the patterns of the other variables that have been shown. A temporal analysis of the spatial distribution showed that these patterns are constantly shifting. During the simulation, such patterns are headed towards various directions and are most pronounced during the day. There is no explicit tendency to a decrease or increase here. We assume that these patterns are caused by atmospheric dynamics rather than surface properties. Nevertheless,



**Figure 5.** Distribution of the ensemble mean dust loading in the top snow layer in SDS (a) and the ensemble mean difference in diffuse surface albedo between SDS and REF (b) on March 29, 2018, 8 UTC.



**Figure 6.** Distribution of the ensemble mean differences in surface shortwave net radiation flux (a), surface temperature (b), snow depth (c), and total precipitation (d), between SDS and REF on March 29, 2018, 8 UTC.

582 on average, a slightly higher surface temperature is apparent in SDS. The mean differ-  
 583 ence in surface temperature over the whole area is 0.03 K. The regional surface temper-  
 584 ature difference between SDS and REF is 0.07 K in A and 0.06 K in B. In the latter re-  
 585 gion, the warming reaches locally up to 2.72 K. The feedback in 2m temperature has very  
 586 similar patterns compared to the surface temperature (not shown). However, the am-  
 587 plitude mostly reaches only half as large values as the feedback of the surface temper-  
 588 ature. The spatially averaged 2m temperature difference in the whole study region is 0.01 K,  
 589 0.03 K in region A, and 0.04 K in region B, which is quite small.

590 The variation in snow depth is among other factors strongly influenced by precip-  
 591 itation patterns. Differences in snow depth and total precipitation are shown in Figure 6c  
 592 and Figure 6d, respectively. In particular, the patterns of both variables on Russian ter-  
 593 ritory, Belarus, and Ukraine match up very accurately. This allows the assumption that  
 594 random changes in precipitation patterns cause these deviations in snow depth. Alter-  
 595 nately, both an increase and a decrease in snow depth occur, with the decrease predom-  
 596 inating in Belarus. This decrease explains the reduction in surface albedo at this loca-  
 597 tion. A thinning of the snow pack reduces the surface albedo, since the ground under-  
 598 neath contributes to a larger extent to the overall albedo. The reduction in surface albedo  
 599 here relates only to a negligible extent to the deposition of mineral dust. However, there  
 600 are widespread areas where a modification in snow depth cannot be accounted for by the  
 601 changes in precipitation. They can be attributed to the perturbation of the optical prop-  
 602 erties of snow due to mineral dust. They coincide with the decrease in surface albedo  
 603 in SDS. For instance, a reduction in snow depth is mainly observed in the Caucasus Moun-  
 604 tains and the mountains further south and east. Furthermore, a decrease in snow depth  
 605 near the snow line is mainly apparent. Again, an exception is an area in Russia north-  
 606 east of the Black Sea. Here an increase in precipitation explains the increase in snow depth  
 607 and surface albedo. The mean difference in snow depth over the whole study region at

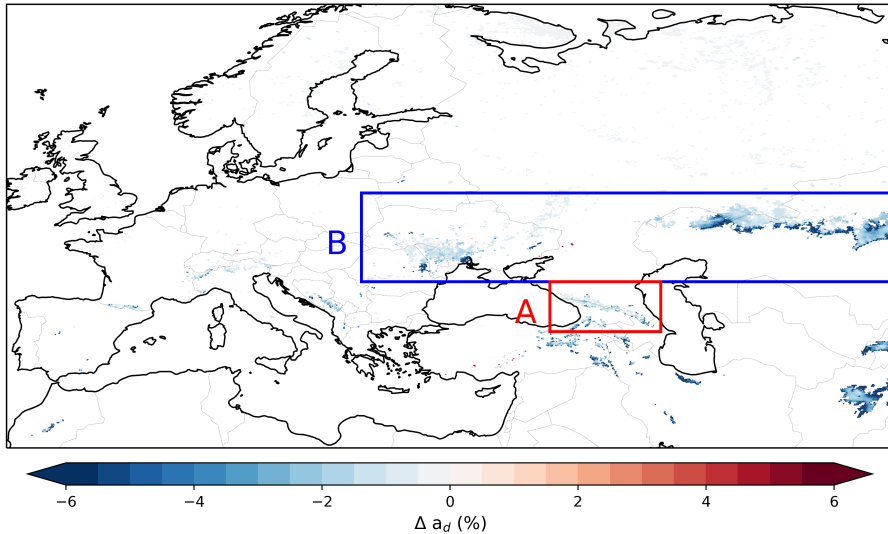


**Figure 7.** Spatial distribution of statistically significant ensemble mean differences between SDS and REF in diffuse surface albedo on March 29, 2018, 8 UTC.

608  $t_{176}$  is  $-0.1$  cm. The strongest local feedback of snow depth is in the French Alps, result-  
 609 ing in a reduction of  $-10.2$  cm. Hence, although the temperature changes appear small,  
 610 the snow depth decreases substantially.

611 The distributions in Figure 5 and Figure 6 show that there are direct feedbacks on  
 612 several variables due to mineral dust deposition. Therefore, a relatively clear and consist-  
 613 ent pattern appears. The difference in snow depth shows a cumulative effect of miner-  
 614 al dust on snow cover. Therefore, a relatively clear and consistent pattern appears. In  
 615 contrast, the differences in net shortwave radiation flux, surface temperature, and 2m  
 616 temperature show an instantaneous effect. Various other influences, such as atmospheric  
 617 dynamics can interfere with these instantaneous mineral dust effects. To assess the sig-  
 618 nificance of our results, we applied the Wilcoxon signed-rank test (Wilcoxon, 1945) and  
 619 the false detection rate control of Wilks (2016) on the surface albedo differences. Fig-  
 620 ure 7 shows the significant surface albedo differences between SDS and REF at  $t_{176}$ . We  
 621 found that only the reduction in surface albedo is statistically significant and caused by  
 622 mineral dust deposition. These significant reductions are mainly limited to the regions  
 623 A and B and some mountain ranges in Eurasia. The strongest signals occur mainly where  
 624 the snow cover is particularly thin, e.g., in Kazakhstan. The mean significant reduction  
 625 in surface albedo at  $t_{176}$  is  $-2.2\%$  over the whole study area, and  $-1.9\%$  and  $-2.3\%$   
 626 in regions A and B, respectively. Increases in surface albedo in our simulation results  
 627 are not statistically significant.

### 628 3.4 Local Implications on The Atmosphere and Land Surface

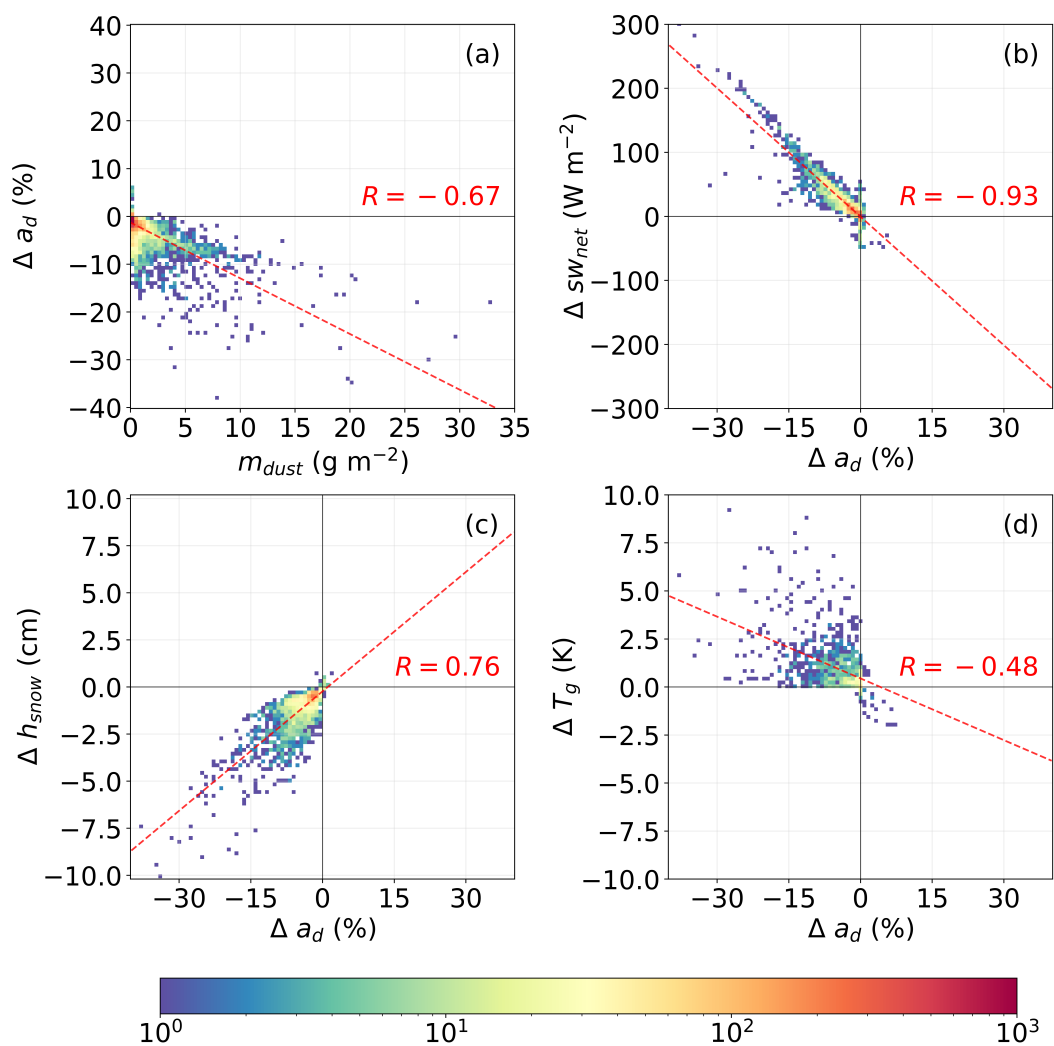
629 In this section, we examine statistical relationships between snow-darkening and  
 630 the differences in atmospheric and land surface variables. Here, our analysis is based on  
 631 statistically significant results only. Figure 8 shows the statistical relationships between  
 632 mineral dust deposition and the impact on surface albedo (a). Furthermore, it shows the  
 633 relationship between the impact on surface albedo and the impact on the variables sur-  
 634 face shortwave net radiation flux (b), snow depth (c), and surface temperature (d). The  
 635 four density scatter plots illustrate the frequency of the occurrences at  $t_{176}$  throughout  
 636 the whole simulation domain. In addition, the linear regression line is indicated as dashed  
 637 red line.

Figure 8a shows that the reduction in surface albedo cannot be explained directly from mineral dust deposition only. The Pearson R correlation coefficient is -0.67 and the results scatter throughout the lower half of the figure. For example, there are many locations where the mineral dust deposition is below  $1 \text{ g m}^{-2}$ , but the reduction in surface albedo reaches an extend of  $-15\%$ . On the other hand, there are locations where the mineral dust deposition is above  $3 \text{ g m}^{-2}$ , but the albedo is affected by less than  $-1\%$ . A clear linear relationship exists between the feedback in surface shortwave net radiation flux and reduction in surface albedo (Figure 8b). Here, the correlation coefficient is -0.93. Hence, a reduction in surface albedo is associated with a clear enhancement of solar energy absorption. Biases in the results can arise in this comparison if the cloud cover differs between SDS and REF. We further found a linear relationship between melting of snow and reduction in surface albedo (Figure 8c). The comparison results in a correlation coefficient of 0.76. Since the coefficient is not close to unity, it suggests that other factors also have an influence on melting. Since we found the strongest feedback in areas near the snow line, where snow cover is patchy and thin, we assume a dependence of the variables on the prevailing snow depth. We discuss this further below. We found the weakest correlation between the feedback of surface temperature (Figure 8d) and 2m temperature (latter not shown) to surface albedo. The correlation coefficients are -0.48 and -0.54, respectively. As previously indicated in the spatial analysis, the two variables have weak feedbacks to snow-darkening, which in turn are easily superimposed by other signals.

Figure 9 represents a similar illustration as Figure 8. In this case, however, the feedbacks of surface albedo (a), surface shortwave net radiation flux (b), snow depth (c), and surface temperature (d) are compared to the prevailing snow depth. We cannot derive any linear relationship here. However, we can identify a dependence of the feedbacks. The intensity is particularly strong at shallow snow depths. This is most noticeable when considering the reduction in surface albedo and the increase in surface temperature. The former shows strong signals with shallow and deep snow cover. However, it appears that the reduction is most pronounced at a snow cover of a few centimeters. We believe that the snow-albedo feedback plays a larger role here. The amplification of the feedback due to the uncovering of the darker ground below the snow. The same process probably causes the slight increase in the absorption of shortwave radiation at shallow snow depths. Furthermore, the surface temperature shows feedbacks almost exclusively at low snow depths of a few centimeters. It is important to consider that the analysed snow depth is an ensemble mean. This means that it is possible that in individual runs the thin snow cover has already melted due to the mineral dust. The exposed land surface can then heat up more (several degrees) in contrast to the snow-covered surfaces. This explains the large dependence of surface temperature changes on snow depth. The effect on snow melting, in contrast, shows a smaller dependence on the current snow depth. Melting is intensified when the snow cover is thin, but strong feedbacks can also occur with deep snow cover of 1 m.

We demonstrate the dependence on the state of snow cover by means of the quantification of the feedbacks in the regions A and B. Table 1 displays the spatial averages of the significant differences between SDS and REF in surface shortwave net radiation flux, snow depth, surface temperature, and 2m temperature. The spatial mean of the corresponding surface albedo differences are presented alongside.

Region A includes the Caucasus Mountains. Thus, the terrain is complex. The snow cover is rather thick and closed. The impact on absorption of shortwave radiation is stronger in region A. There is an increase in surface shortwave net radiation flux by  $18.47 \text{ W m}^{-2}$ . This additional energy is mainly reflected in snow melt. The snow depth is reduced here by  $-1.36 \text{ cm}$  on average. The surface temperature and the 2m temperature, however, show a weaker signal in region A. In region B, which is mainly characterized by flat area in Kazakhstan, the reduction in snow depth is lower with a mean decrease of  $-0.60 \text{ cm}$ . The increase in surface shortwave net radiation flux amounts  $15.96 \text{ W m}^{-2}$ . However, there is a stronger warming of the land surface and the near-surface atmosphere in region B.



**Figure 8.** Density scatter plots of significant local ensemble mean differences in diffuse surface albedo between SDS and REF in relation to dust loading in the top snow layer in SDS (a), the significant local differences in surface shortwave net radiation flux (b), snow depth (c), surface temperature (d), in relation to differences in diffuse surface albedo between SDS and REF on March 29, 2018, 8 UTC.

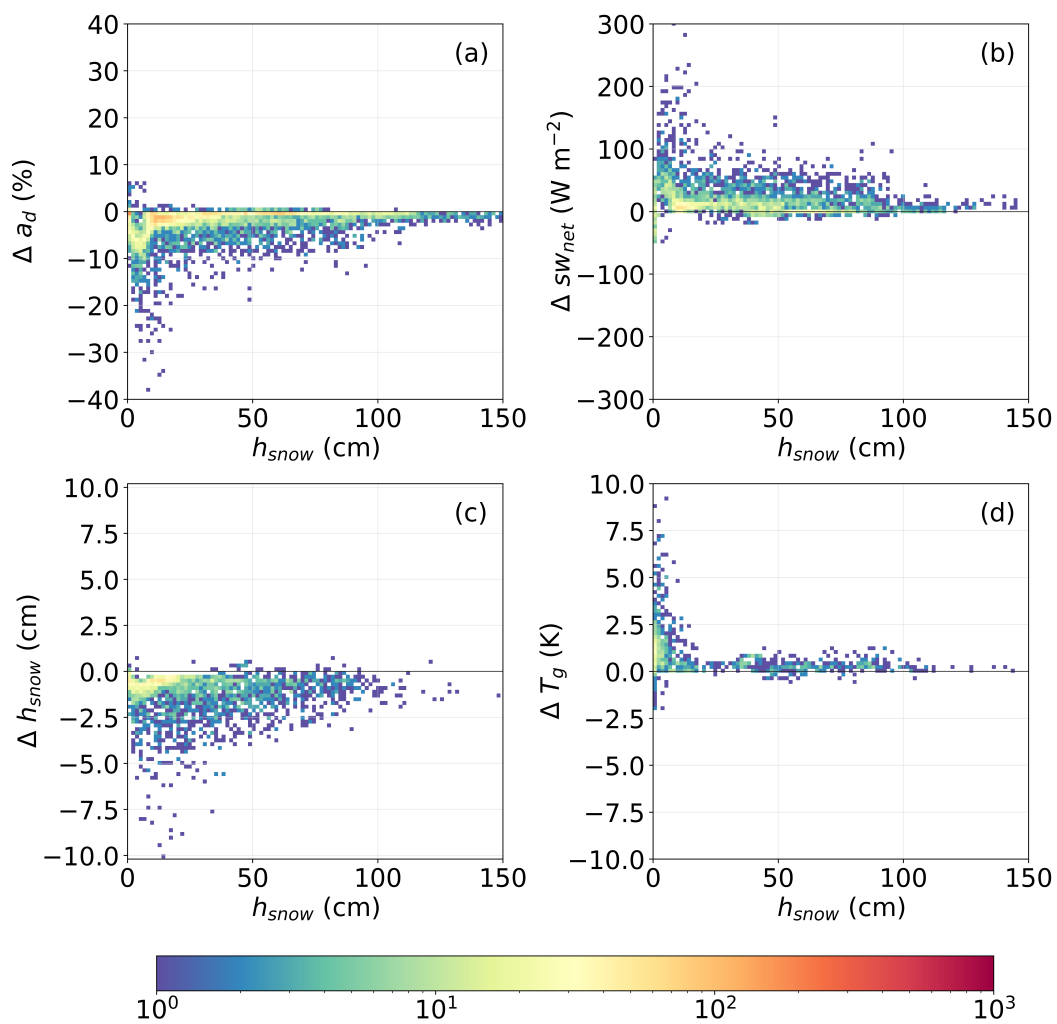


**Figure 9.** Density scatter plots of significant local differences between SDS and REF in diffuse surface albedo (a), surface shortwave net radiation flux (b), snow depth (c), surface temperature (d), in relation to the apparent snow depth on March 29, 2018, 8 UTC.

**Table 1.** Spatial average of the statistically significant feedback in surface shortwave net radiation flux  $sw_{net}$ , snow depth  $h_{snow}$ , surface temperature  $T_g$ , and 2m temperature  $T_{2m}$  in region A and B and associated changes in diffuse surface albedo after 176 hours of simulation on March 29, 2018, 8 UTC.

Var	Region	Mean of significant differences	Mean of associated surface albedo differences
$\Delta sw_{net}$	A	18.47 W m <sup>-2</sup>	-2.72 %
	B	15.96 W m <sup>-2</sup>	-2.50 %
$\Delta h_{snow}$	A	-1.36 cm	-2.83 %
	B	-0.60 cm	-3.41 %
$\Delta T_g$	A	0.69 K	-3.96 %
	B	0.92 K	-4.50 %
$\Delta T_{2m}$	A	0.30 K	-4.57 %
	B	0.49 K	-4.20 %

693 The increase in surface temperature and 2m temperature is on average 0.92 K and 0.49 K,  
694 respectively.

#### 695 4 Conclusions

696 We improved the model ICON-ART by implementing a new snow albedo parametriza-  
697 tion following Wiscombe and Warren (1980) and Warren and Wiscombe (1980). The new  
698 developments enable the computation of a spectral snow albedo in 18 shortwave bands.  
699 We included mineral dust optical properties of ICON-ART in our developments to in-  
700 vestigate its impact on the snow albedo. In our simulations, the deposition of mineral  
701 dust affects the optical properties of the snow surface online. Postdepositional processes  
702 such as sinking of mineral dust particles into the snowpack and resurfacing are accounted  
703 for.

704 We conducted a case study to analyze the impact of mineral dust deposition on the  
705 spectral snow albedo during a large Saharan dust deposition event. This event occurred  
706 in spring 2018 and affected snow surfaces in Eastern Europe and western parts of Asia.  
707 Emission, transport, deposition, and impact of mineral dust were computed online in the  
708 experiment. We applied an ensemble simulation with a total of 80 ensemble members  
709 to investigate the impact during this intensive event. Furthermore, we obtained evidence  
710 of statistical significance by applying the Wilcoxon signed-rank test (Wilcoxon, 1945)  
711 and the significance evaluation described by Wilks (2016).

712 We analyzed the spatial distribution of mineral dust and associated feedbacks dur-  
713 ing this event in Eurasia to answer the question whether the distribution of mineral dust  
714 results in the formation of particularly vulnerable regions. We found that dust loading  
715 in snow is spatially highly variable and affects certain regions with particular severity.  
716 Mountainous regions and a relatively flat area in Kazakhstan were primarily affected.  
717 The former showed particularly severe contamination with dust particles, especially on  
718 the southwestern slopes. The latter is probably strongly influenced due to the proxim-  
719 ity to dust sources and melting processes at the snow line. Here the snow-albedo feed-  
720 back plays a larger role. Through the particularly thin snow layer in this region, the darker  
721 ground below the snow gets more influence in the total albedo. It is therefore highly im-  
722 portant to simulate aerosol emission, transport and deposition online to achieve a proper  
723 distribution of the mineral dust. The temporal evolution of the snow cover plays an im-  
724 portant role, as it determines whether the aerosols sink in with new snowfall or concen-  
725 trate on the snow surface due to snow melt. Our results show that larger amounts of clean  
726 fresh snow can rapidly offset the effects of mineral dust.

727 The second question we set out to answer is: How intense can the feedbacks in the  
 728 land surface and the atmosphere be during the severe dust event? We found that the min-  
 729 eral dust causes a statistically significant reduction in surface albedo and snow depth as  
 730 well as a statistically significant increase in surface shortwave net radiation flux, surface  
 731 temperature, and 2m temperature. In individual locations, very strong feedbacks can oc-  
 732 cur. In the case of the surface albedo, for example, the reduction extended to  $-38.4\%$   
 733 and the reduction in snow depth to  $-10.2\text{ cm}$ . However, these are extreme cases. On av-  
 734 erage, the reduction in surface albedo was  $-2.7\%$  and the reduction in snow depth was  
 735  $-1.36\text{ cm}$  in the Caucasus region. The increase in shortwave net radiation flux in the re-  
 736 gion averaged  $18.47\text{ W m}^{-2}$ .

737 The final question we address in this study is which surface and atmospheric vari-  
 738 ables are most strongly affected during this event. We found a strong regional depen-  
 739 dence of the feedbacks, mainly due to the state of the snow cover. In a thick, closed snow  
 740 pack, additional absorbed shortwave radiation leads to snow melt. We found this rela-  
 741 tionship mainly in mountainous areas. With thin snow cover, the radiative forcing leads  
 742 to warming of the surface and air temperature instead. The reason for this is that dust  
 743 deposition coincides with patchy and thin snow. Snow melt also occurs in these areas,  
 744 but the solar energy is more likely to melt away the snow cover and reach the land sur-  
 745 face. The energy that reaches the ground causes strong warming of the surface. How-  
 746 ever, this feedback remains rather small compared to the effects on surface albedo, short-  
 747 wave net radiation flux, and snow depth. In the region along the snow line, the mean  
 748 increase in surface temperature was  $0.9\text{ K}$  and the increase in 2m temperature was  $0.49\text{ K}$ .

749 In conclusion, to estimate the responses to the snow-darkening effect, it is impor-  
 750 tant to consider the aspects of exposure to dust deposition, altitude, and snow coverage  
 751 of the study region. Mountain ranges are especially affected by mineral dust deposition,  
 752 in particular the south facing slopes in this case. The resulting response is mainly the  
 753 reduction in snow cover. Moreover, the snow line in Eurasia is one of the most sensitive  
 754 regions despite the flat area since the snow cover fraction is small. This leads mainly to  
 755 a surface warming because of the accelerated retreat of the snow line to the north and  
 756 exposure of the darker ground.

## 757 Acknowledgments

758 The work described in this paper has received funding from the Initiative and Network-  
 759 ing Fund of the Helmholtz Association through the project “Advanced Earth System Mod-  
 760 elling Capacity (ESM)”. Furthermore, we kindly thank the DWD for providing the dust  
 761 initialization data. Many thanks to Jan Cermak for his advice regarding the treatment  
 762 of shortwave radiation in spectral bands. Special thanks to Sven Werchner for his sup-  
 763 port in the development of the ICON-ART code. Many thanks to Oliver Gutjahr for his  
 764 recommendation on the treatment of the false discovery rate.

765 Author contributions: Anika Rohde and Bernhard Vogel implemented the process  
 766 of snow-darkening in ICON-ART and performed the simulations. Heike Vogel gathered  
 767 and prepared the initialization data. Anika Rohde, Bernhard Vogel, Heike Vogel, Gho-  
 768 lam Ali Hoshyaripour and Christoph Kottmeier were involved in the discussion of the  
 769 results. Anika Rohde, Bernhard Vogel, Heike Vogel and Gholam Ali Hoshyaripour pre-  
 770 pared the manuscript with significant contributions from all authors.

771 Competing interests: The authors declare that they have no conflict of interest.

772 Data and code availability: The used ICON-ART code is license protected and can  
 773 be accessed by request to the corresponding author. Data and post-processing scripts  
 774 are also available upon request.

## 775 References

776 Aoki, T., Motoyoshi, H., Kodama, Y., Yasunari, T. J., Sugiura, K., & Kobayashi,  
 777 H. (2006). Atmospheric aerosol deposition on snow surfaces and its effect on

- 778 albedo. *Scientific Online Letters on the Atmosphere*, 2(0), 13–16.
- 779 Barkan, J., & Alpert, P. (2020). Red snow occurrence in eastern europe. a case  
780 study. *Weather*, 75(2), 45–48.
- 781 Bartelt, P., & Lehning, M. (2002). A physical snowpack model for the swiss  
782 avalanche warning part i: numerical model. *Cold Regions Science and Technol-*  
783 *ogy*, 35(3), 123–145.
- 784 Brun, E., David, P., Sudul, M., & Brunot, G. (1992). A numerical model to sim-  
785 ulate snow-cover stratigraphy for operational avalanche forecasting. *Journal of*  
786 *Glaciology*, 38(128), 13–22.
- 787 Bryant, A. C., Painter, T. H., Deems, J. S., & Bender, S. M. (2013). Impact of dust  
788 radiative forcing in snow on accuracy of operational runoff prediction in the  
789 upper colorado river basin. *Geophysical Research Letters*, 40(15), 3945–3949.
- 790 Deems, J. S., Painter, T. H., Barsugli, J. J., Belnap, J., & Udall, B. (2013). Com-  
791 bined impacts of current and future dust deposition and regional warming  
792 on colorado river basin snow dynamics and hydrology. *Hydrology and Earth*  
793 *System Sciences*, 17(11), 4401–4413.
- 794 Di Mauro, B., Garzonio, R., Rossini, M., Filippa, G., Pogliotti, P., Galvagno, M.,  
795 ... Colombo, R. (2019). Saharan dust events in the european alps: role in  
796 snowmelt and geochemical characterization. *The Cryosphere*, 13(4), 1147–  
797 1165.
- 798 Doms, G., Förstner, J., Heise, E., Herzog, H., Mironov, D., Raschendorfer, M., ...  
799 others (2018). A description of the nonhydrostatic regional cosmo model. part  
800 ii: Physical parameterization. *Deutscher Wetterdienst, Offenbach, Germany*.
- 801 Donth, T., Jäkel, E., Ehrlich, A., Heinold, B., Schacht, J., Herber, A., ... Wendisch,  
802 M. (2020). Combining atmospheric and snow radiative transfer models to  
803 assess the solar radiative effects of black carbon in the arctic. *Atmospheric*  
804 *Chemistry and Physics*, 20(13), 8139–8156.
- 805 Dumont, M., Brun, E., Picard, G., Michou, M., Libois, Q., Petit, J. R., ... Josse,  
806 B. (2014). Contribution of light-absorbing impurities in snow to greenland’s  
807 darkening since 2009. *Nature Geoscience*, 7(7), 509–512.
- 808 Dumont, M., Tuzet, F., Gascoïn, S., Picard, G., Kutuzov, S., Lafaysse, M., ...  
809 Painter, T. H. (2020). Accelerated snow melt in the russian caucasus moun-  
810 tains after the saharan dust outbreak in march 2018. *Journal of Geophysical*  
811 *Research: Earth Surface*, 125(9), e2020JF005641.
- 812 Essery, R., Best, M., & Cox, P. (2001, 20 August 2001). Moses 2.2 technical docu-  
813 mentation [Report].
- 814 Flanner, M. G., Liu, X., Zhou, C., Penner, J. E., & Jiao, C. (2012). Enhanced solar  
815 energy absorption by internally-mixed black carbon in snow grains. *Atmo-*  
816 *spheric Chemistry and Physics*, 12(10), 4699–4721.
- 817 Flanner, M. G., & Zender, C. S. (2005). Snowpack radiative heating: Influence on ti-  
818 betan plateau climate. *Geophysical Research Letters*, 32(6).
- 819 Flanner, M. G., Zender, C. S., Hess, P. G., Mahowald, N. M., Painter, T. H., Ra-  
820 manathan, V., & Rasch, P. (2009). Springtime warming and reduced snow  
821 cover from carbonaceous particles. *Atmospheric Chemistry and Physics*, 9(7),  
822 2481–2497.
- 823 Flanner, M. G., Zender, C. S., Randerson, J. T., & Rasch, P. J. (2007). Present-day  
824 climate forcing and response from black carbon in snow. *Journal of Geophysi-*  
825 *cal Research: Atmospheres*, 112(D11).
- 826 Fujita, K. (2007). Effect of dust event timing on glacier runoff: sensitivity analysis  
827 for a tibetan glacier. *Hydrological Processes*, 21(21), 2892–2896.
- 828 Gabbi, J., Huss, M., Bauder, A., Cao, F., & Schwikowski, M. (2015). The impact  
829 of saharan dust and black carbon on albedo and long-term mass balance of an  
830 alpine glacier. *The Cryosphere*, 9(4), 1385–1400.
- 831 Gasch, P., Rieger, D., Walter, C., Khain, P., Levi, Y., Knippertz, P., & Vogel, B.  
832 (2017). Revealing the meteorological drivers of the september 2015 severe

- 833 dust event in the eastern mediterranean. *Atmospheric Chemistry and Physics*,  
834 *17*(22), 13573.
- 835 Gautam, R., Hsu, N. C., Lau, W. K. M., & Yasunari, T. J. (2013). Satellite observa-  
836 tions of desert dust-induced himalayan snow darkening. *Geophysical Research*  
837 *Letters*, *40*(5), 988–993.
- 838 Giorgetta, M. A., Brokopf, R., Crueger, T., Esch, M., Fiedler, S., Helmert, J., ...  
839 Stevens, B. (2018). Icon-a, the atmosphere component of the icon earth system  
840 model: I. model description. *Journal of Advances in Modeling Earth Systems*,  
841 *10*(7), 1613–1637.
- 842 Hansen, J. (2005). Efficacy of climate forcings. *Journal of Geophysical Research: At-*  
843 *mospheres*, *110*(D18).
- 844 Hansen, J., & Nazarenko, L. (2004). Soot climate forcing via snow and ice albedo.  
845 *Proceedings of the National Academy of Sciences of the United States of*  
846 *America*, *101*(2), 423–428.
- 847 Hoshyaripour, G. A., Bachmann, V., Förstner, J., Steiner, A., Vogel, H., Wagner, F.,  
848 ... Vogel, B. (2019). Effects of particle nonsphericity on dust optical prop-  
849 erties in a forecast system: Implications for model-observation comparison.  
850 *Journal of Geophysical Research: Atmospheres*, *124*(13), 7164–7178.
- 851 Jacobi, H. W., Lim, S., Ménégos, M., Ginot, P., Laj, P., Bonasoni, P., ... Arnaud,  
852 Y. (2015). Black carbon in snow in the upper himalayan khumbu valley,  
853 nepal: observations and modeling of the impact on snow albedo, melting, and  
854 radiative forcing. *The Cryosphere*, *9*(4), 1685–1699.
- 855 Jacobson, M. Z. (2004). Climate response of fossil fuel and biofuel soot, accounting  
856 for soot’s feedback to snow and sea ice albedo and emissivity. *Journal of Geo-*  
857 *physical Research: Atmospheres*, *109*(D21).
- 858 Jäkel, E., Carlsen, T., Ehrlich, A., Wendisch, M., Schäfer, M., Rosenburg, S., ...  
859 Rohde, A. (2021). Measurements and modeling of optical-equivalent snow  
860 grain sizes under arctic low-sun conditions. *Remote Sensing*, *13*(23).
- 861 Kaspari, S., Painter, T. H., Gysel, M., Skiles, S. M., & Schwikowski, M. (2014).  
862 Seasonal and elevational variations of black carbon and dust in snow and ice  
863 in the solu-khumbu, nepal and estimated radiative forcings. *Atmospheric*  
864 *Chemistry and Physics*, *14*(15), 8089–8103.
- 865 Lau, W. K. M., Sang, J., Kim, M. K., Kim, K. M., Koster, R. D., & Yasunari, T. J.  
866 (2018). Impacts of snow darkening by deposition of light-absorbing aerosols on  
867 hydroclimate of eurasia during boreal spring and summer. *Journal of Geophys-*  
868 *ical Research: Atmospheres*, *123*(16), 8441–8461.
- 869 Lehning, M., Bartelt, P., Brown, B., & Fierz, C. (2002). A physical snowpack model  
870 for the swiss avalanche warning part iii: meteorological forcing, thin layer  
871 formation and evaluation. *Cold Regions Science and Technology*, *35*, 169–184.
- 872 Lehning, M., Bartelt, P., Brown, B., Fierz, C., & Satyawali, P. (2002). A physical  
873 snowpack model for the swiss avalanche warning part ii: Snow microstructure.  
874 *Cold Regions Science and Technology*, *35*(3), 147–167.
- 875 Lehning, M., Bartelt, P., Brown, B., Russi, T., Stockli, U., & Zimmerli, M. (1999).  
876 Snowpack model calculations for avalanche warning based upon a new network  
877 of weather and snow stations. *Cold Regions Science and Technology*, *30*(1-3),  
878 145–157.
- 879 Li, X., Kang, S., He, X., Qu, B., Tripathee, L., Jing, Z., ... Li, C. (2017). Light-  
880 absorbing impurities accelerate glacier melt in the central tibetan plateau. *Sci-*  
881 *ence of The Total Environment*, *587-588*, 482–490.
- 882 Libois, Q., Picard, G., France, J. L., Arnaud, L., Dumont, M., Carmagnola, C. M.,  
883 & King, M. D. (2013). Influence of grain shape on light penetration in snow.  
884 *The Cryosphere*, *7*(6), 1803–1818.
- 885 Machulskaya, E. E., & Lykosov, V. N. (2008). An advanced snow parameterization  
886 for models of atmospheric circulation. *COSMO Newsletter*, *8*, 10–16.
- 887 Marmureanu, L., Marin, C. A., Andrei, S., Antonescu, B., Ene, D., Boldeanu, M., ...

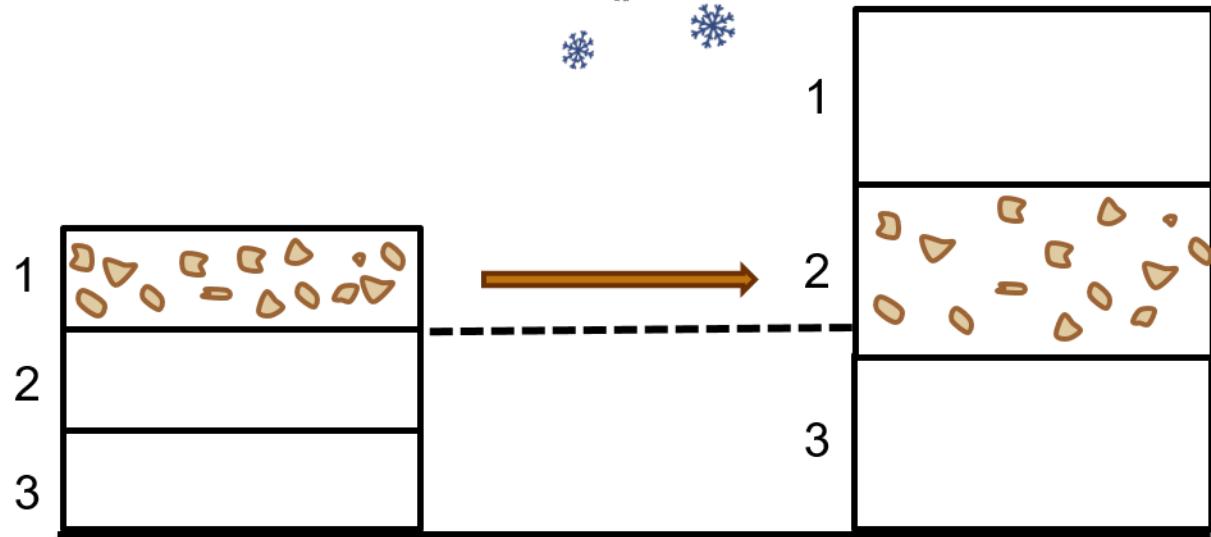
- 888 Levei, E. (2019). Orange snow—a saharan dust intrusion over romania during  
889 winter conditions. *Remote Sensing*, *11*(21).
- 890 Meinander, O., Kazadzis, S., Arola, A., Riihelä, A., Räisänen, P., Kivi, R., . . .  
891 Hautecoeur, O. (2013). Spectral albedo of seasonal snow during intensive  
892 melt period at sodankylä, beyond the arctic circle. *Atmospheric Chemistry and*  
893 *Physics*, *13*(7), 3793–3810.
- 894 Mie, G. (1908). Beiträge zur optik trüber medien, speziell kolloidaler metallösungen.  
895 *Annalen der Physik*, *330*(3), 377–445.
- 896 Mlawer, E. J., Taubman, S. J., Brown, P. D., Iacono, M. J., & Clough, S. A.  
897 (1997). Radiative transfer for inhomogeneous atmospheres: Rrtm, a vali-  
898 dated correlated-k model for the longwave. *Journal of Geophysical Research:*  
899 *Atmospheres*, *102*(D14), 16663–16682.
- 900 Monteiro, A., Basart, S., Kazadzis, S., Votsis, A., Gkikas, A., Vandenbussche, S., . . .  
901 Nickovic, S. (2022). Multi-sectoral impact assessment of an extreme african  
902 dust episode in the eastern mediterranean in march 2018. *Sci Total Environ*,  
903 *843*, 156861. doi: 10.1016/j.scitotenv.2022.156861
- 904 Nagorski, S. A., Kaspari, S. D., Hood, E., Fellman, J. B., & Skiles, S. M. (2019).  
905 Radiative forcing by dust and black carbon on the juneau icefield, alaska.  
906 *Journal of Geophysical Research: Atmospheres*, *124*(7), 3943–3959.
- 907 Painter, T. H., Deems, J. S., Belnap, J., Hamlet, A. F., Landry, C. C., & Udall, B.  
908 (2010). Response of colorado river runoff to dust radiative forcing in snow.  
909 *Proceedings of the National Academy of Sciences of the United States of Amer-*  
910 *ica*, *107*(40), 17125–17130.
- 911 Peltoniemi, J. I., Gritsevich, M., Hakala, T., Dagsson-Waldhauserová, P., Arnalds,  
912 O., Anttila, K., . . . de Leeuw, G. (2015). Soot on snow experiment: bidirec-  
913 tional reflectance factor measurements of contaminated snow. *The Cryosphere*,  
914 *9*(6), 2323–2337.
- 915 Qian, Y., Gustafson, W. I., Leung, L. R., & Ghan, S. J. (2009). Effects of soot-  
916 induced snow albedo change on snowpack and hydrological cycle in western  
917 united states based on weather research and forecasting chemistry and regional  
918 climate simulations. *Journal of Geophysical Research: Atmospheres*, *114*(D3).
- 919 Rahimi, S., Liu, X., Zhao, C., Lu, Z., & Lebo, Z. J. (2020). Examining the atmo-  
920 spheric radiative and snow-darkening effects of black carbon and dust across  
921 the rocky mountains of the united states using wrf-chem. *Atmospheric Chem-*  
922 *istry and Physics*, *20*(18), 10911–10935.
- 923 Rieger, D., Bangert, M., Bischoff-Gauss, I., Förstner, J., Lundgren, K., Reinert,  
924 D., . . . Vogel, B. (2015). Icon-art 1.0 – a new online-coupled model system  
925 from the global to regional scale. *Geoscientific Model Development*, *8*(6),  
926 1659–1676.
- 927 Rieger, D., Steiner, A., Bachmann, V., Gasch, P., Förstner, J., Deetz, K., . . . Vogel,  
928 H. (2017). Impact of the 4 april 2014 saharan dust outbreak on the photo-  
929 voltaic power generation in germany. *Atmospheric Chemistry and Physics*,  
930 *17*(21), 13391–13415.
- 931 Rohde, A. (2021). *The impact of the snow-darkening effect on snow cover and the*  
932 *atmosphere during a major dust event across eurasia* (Doctoral dissertation).  
933 Retrieved from KITopen. (KITopen-ID: 1000141199). Karlsruhe: Karlsruhe  
934 Institute of Technologie (KIT).
- 935 Sarangi, C., Qian, Y., Rittger, K., Bormann, K. J., Liu, Y., Wang, H., . . . Painter,  
936 T. H. (2019). Impact of light-absorbing particles on snow albedo darkening  
937 and associated radiative forcing over high-mountain asia: high-resolution wrf-  
938 chem modeling and new satellite observations. *Atmospheric Chemistry and*  
939 *Physics*, *19*(10), 7105–7128.
- 940 Sarangi, C., Qian, Y., Rittger, K., Ruby Leung, L., Chand, D., Bormann, K. J., &  
941 Painter, T. H. (2020). Dust dominates high-altitude snow darkening and melt  
942 over high-mountain asia. *Nature Climate Change*, *10*(11), 1045–1051.

- 943 Schröter, J., Rieger, D., Stassen, C., Vogel, H., Weimer, M., Werchner, S., ...  
 944 Braesicke, P. (2018). Icon-art 2.1: a flexible tracer framework and its ap-  
 945 plication for composition studies in numerical weather forecasting and climate  
 946 simulations. *Geoscientific Model Development*, *11*(10), 4043–4068.
- 947 Shi, T., Cui, J., Chen, Y., Zhou, Y., Pu, W., Xu, X., ... Wang, X. (2021). En-  
 948 hanced light absorption and reduced snow albedo due to internally mixed  
 949 mineral dust in grains of snow. *Atmospheric Chemistry and Physics*, *21*(8),  
 950 6035–6051.
- 951 Skiles, S. M., & Painter, T. H. (2018). Assessment of radiative forcing by light-  
 952 absorbing particles in snow from in situ observations with radiative transfer  
 953 modeling. *Journal of Hydrometeorology*, *19*(8), 1397–1409.
- 954 Skiles, S. M., & Painter, T. H. (2019). Toward understanding direct absorption  
 955 and grain size feedbacks by dust radiative forcing in snow with coupled snow  
 956 physical and radiative transfer modeling. *Water Resources Research*, *55*(8),  
 957 7362–7378.
- 958 Skiles, S. M., Painter, T. H., Belnap, J., Holland, L., Reynolds, R. L., Goldstein,  
 959 H. L., & Lin, J. (2015). Regional variability in dust-on-snow processes and  
 960 impacts in the upper colorado river basin. *Hydrological Processes*, *29*(26),  
 961 5397–5413.
- 962 Solomos, S., Kalivitis, N., Mihalopoulos, N., Amiridis, V., Kouvarakis, G., Gkikas,  
 963 A., ... Marengo, F. (2018). From tropospheric folding to khamsin and foehn  
 964 winds: How atmospheric dynamics advanced a record-breaking dust episode in  
 965 crete. *Atmosphere*, *9*(7).
- 966 Svensson, J., Ström, J., Kivekäs, N., Dkhar, N. B., Tayal, S., Sharma, V. P., ... Li-  
 967 havainen, H. (2018). Light-absorption of dust and elemental carbon in snow  
 968 in the indian himalayas and the finnish arctic. *Atmospheric Measurement*  
 969 *Techniques*, *11*(3), 1403–1416.
- 970 Svensson, J., Virkkula, A., Meinander, O., Kivekas, N., Hannula, H. R., Jarvinen,  
 971 O., ... Lihavainen, H. (2016). Soot-doped natural snow and its albedo - re-  
 972 sults from field experiments. *Boreal Environment Research*, *21*(5-6), 481–503.
- 973 Tuzet, F., Dumont, M., Arnaud, L., Voisin, D., Lamare, M., Larue, F., ... Picard,  
 974 G. (2019). Influence of light-absorbing particles on snow spectral irradiance  
 975 profiles. *The Cryosphere*, *13*(8), 2169–2187.
- 976 Tuzet, F., Dumont, M., Lafaysse, M., Picard, G., Arnaud, L., Voisin, D., ... Morin,  
 977 S. (2017). A multilayer physically based snowpack model simulating direct  
 978 and indirect radiative impacts of light-absorbing impurities in snow. *The*  
 979 *Cryosphere*, *11*(6), 2633–2653.
- 980 Usha, K. H., Nair, V. S., & Babu, S. S. (2020). Modeling of aerosol induced snow  
 981 albedo feedbacks over the himalayas and its implications on regional climate.  
 982 *Climate Dynamics*, *54*(9-10), 4191–4210.
- 983 Vionnet, V., Brun, E., Morin, S., Boone, A., Faroux, S., Le Moigne, P., ...  
 984 Willemet, J. M. (2012). The detailed snowpack scheme crocus and its im-  
 985 plementation in surfex v7.2. *Geoscientific Model Development*, *5*(3), 773–791.
- 986 Vogel, B., Hoose, C., Vogel, H., & Kottmeier, C. (2006, 12). A model of dust trans-  
 987 port applied to the dead sea area. *Meteorologische Zeitschrift*, *15*(6), 611–624.
- 988 Warren, S. G., & Brandt, R. E. (2008). Optical constants of ice from the ultraviolet  
 989 to the microwave: A revised compilation. *Journal of Geophysical Research: At-*  
 990 *mospheres*, *113*(D14).
- 991 Warren, S. G., & Wiscombe, W. J. (1980). A model for the spectral albedo of snow  
 992 2. snow containing atmospheric aerosols. *Journal of the Atmospheric Sciences*,  
 993 *37*(12), 2734–2745.
- 994 Wilcoxon, F. (1945). Individual comparisons by ranking methods. *Biometrics Bul-*  
 995 *letin*, *1*(6).
- 996 Wilks, D. S. (2016). “the stippling shows statistically significant grid points”: How  
 997 research results are routinely overstated and overinterpreted, and what to do

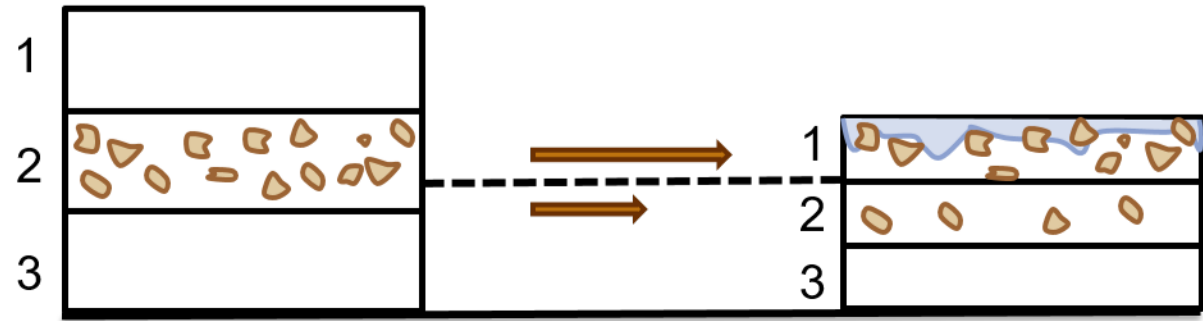
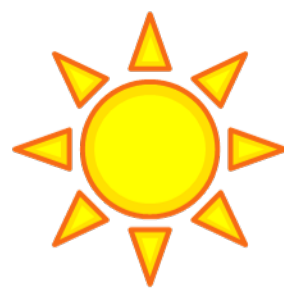
- 998 about it. *Bulletin of the American Meteorological Society*, 97(12), 2263–2273.
- 999 Winker, D., Hunt, W., & Hostetler, C. (2004, 11). Status and performance of the  
1000 caliop lidar. *Proceedings of SPIE - The International Society for Optical Engi-*  
1001 *neering*, 5575.
- 1002 Winker, D. M., Hunt, W. H., & McGill, M. J. (2007). Initial performance assessment  
1003 of caliop. *Geophysical Research Letters*, 34(19).
- 1004 Wiscombe, W. J., & Warren, S. G. (1980). A model for the spectral albedo of snow  
1005 1. pure snow. *Journal of the Atmospheric Sciences*, 37(12), 2712–2733.
- 1006 Wu, L., Gu, Y., Jiang, J. H., Su, H., Yu, N., Zhao, C., . . . Choi, Y.-S. (2018). Im-  
1007 pacts of aerosols on seasonal precipitation and snowpack in california based  
1008 on convection-permitting wrf-chem simulations. *Atmospheric Chemistry and*  
1009 *Physics*, 18(8), 5529–5547.
- 1010 Xu, B., Cao, J., Hansen, J., Yao, T., Joswia, D. R., Wang, N., . . . He, J. (2009).  
1011 Black soot and the survival of tibetan glaciers. *Proceedings of the National*  
1012 *Academy of Sciences of the United States of America*, 106(52), 22114–22118.
- 1013 Yasunari, T. J., Koster, R. D., Lau, W. K. M., & Kim, K.-M. (2015). Impact of  
1014 snow darkening via dust, black carbon, and organic carbon on boreal spring  
1015 climate in the earth system. *Journal of Geophysical Research: Atmospheres*,  
1016 120(11), 5485–5503.
- 1017 Zängl, G., Reinert, D., Rípodas, P., & Baldauf, M. (2015). The icon (icosahedral  
1018 non-hydrostatic) modelling framework of dvd and mpi-m: Description of the  
1019 non-hydrostatic dynamical core. *Quarterly Journal of the Royal Meteorological*  
1020 *Society*, 141(687), 563–579.
- 1021 Zhao, C., Hu, Z., Qian, Y., Ruby Leung, L., Huang, J., Huang, M., . . . Streets,  
1022 D. G. (2014). Simulating black carbon and dust and their radiative forcing  
1023 in seasonal snow: a case study over north china with field campaign measure-  
1024 ments. *Atmospheric Chemistry and Physics*, 14(20), 11475–11491.
- 1025 Zhong, E., Li, Q., Sun, S., Chen, W., Chen, S., & Nath, D. (2017). Improvement of  
1026 a snow albedo parameterization in the snow–atmosphere–soil transfer model:  
1027 evaluation of impacts of aerosol on seasonal snow cover. *Advances in Atmo-*  
1028 *spheric Sciences*, 34(11), 1333–1345.

01\_scheme-dust-transport-in-snow.png.

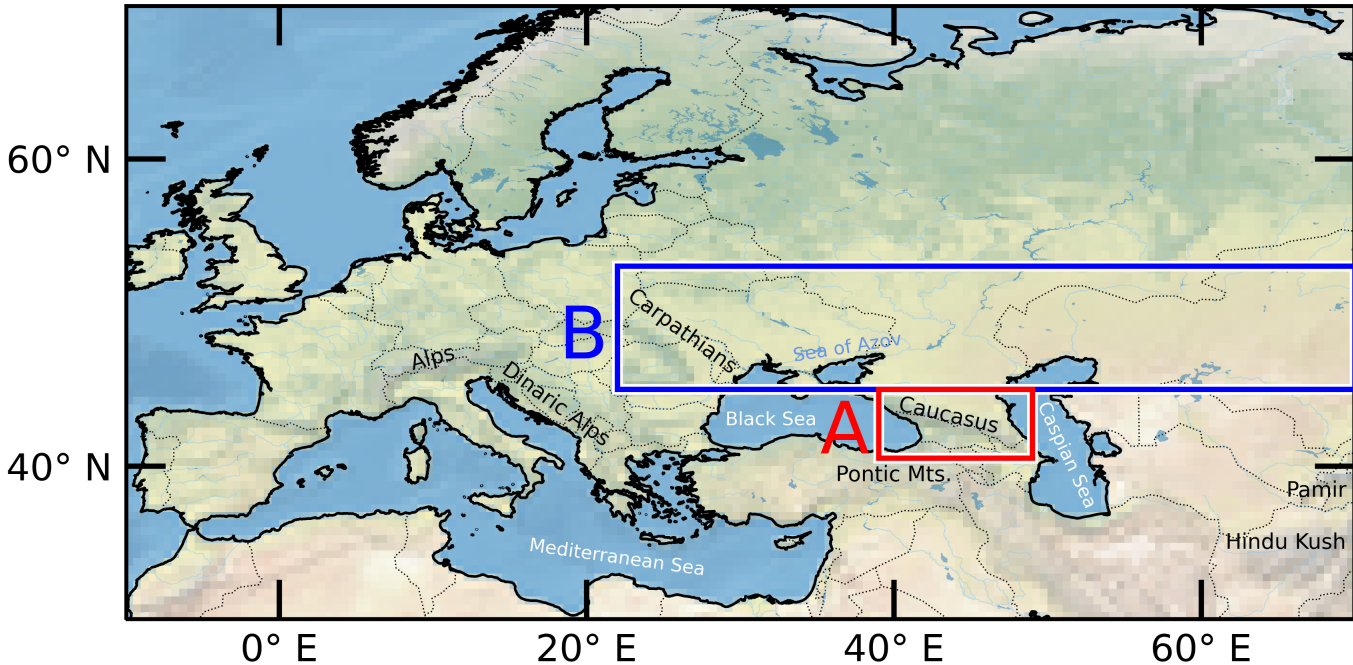
(a)



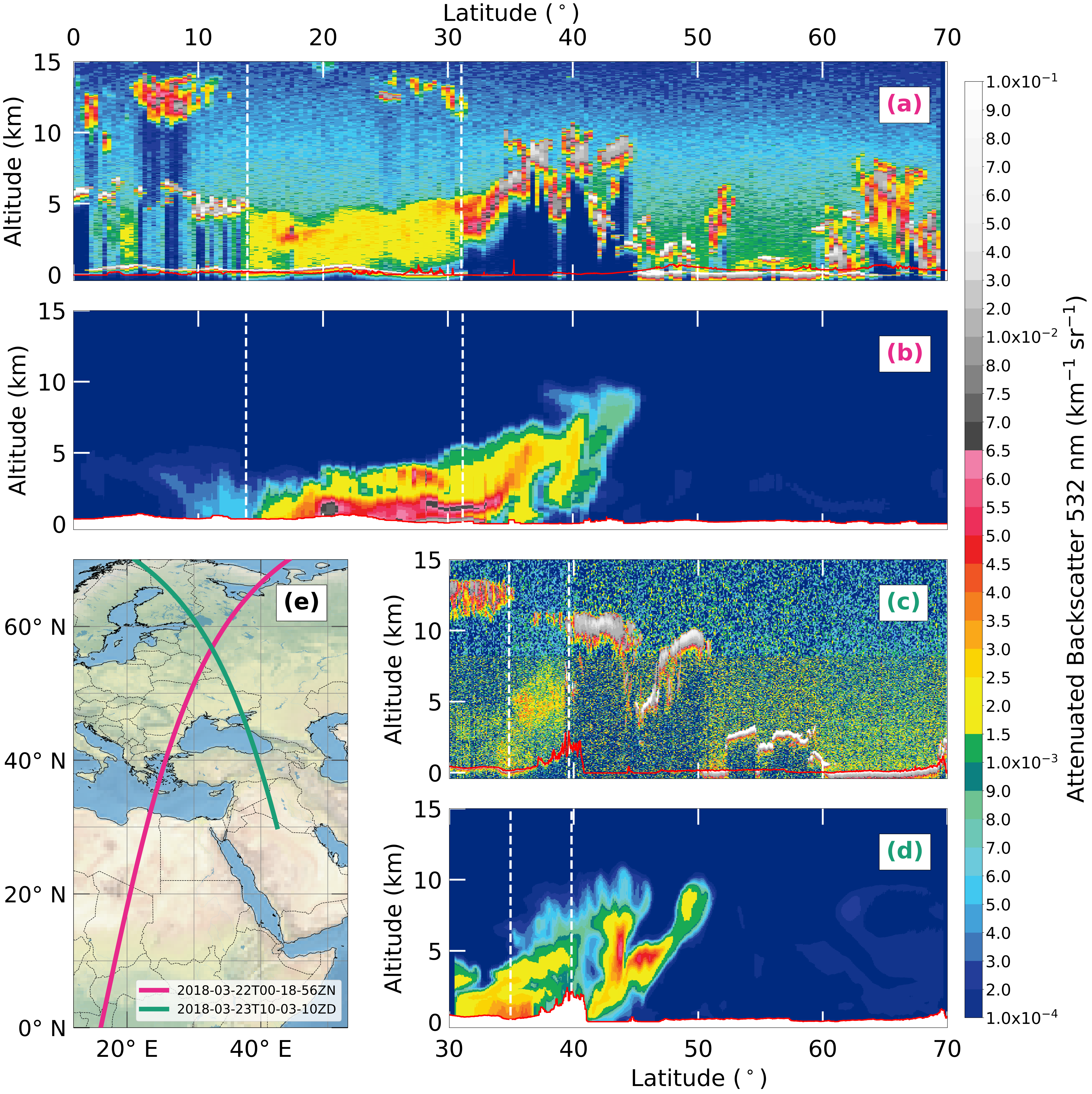
(b)



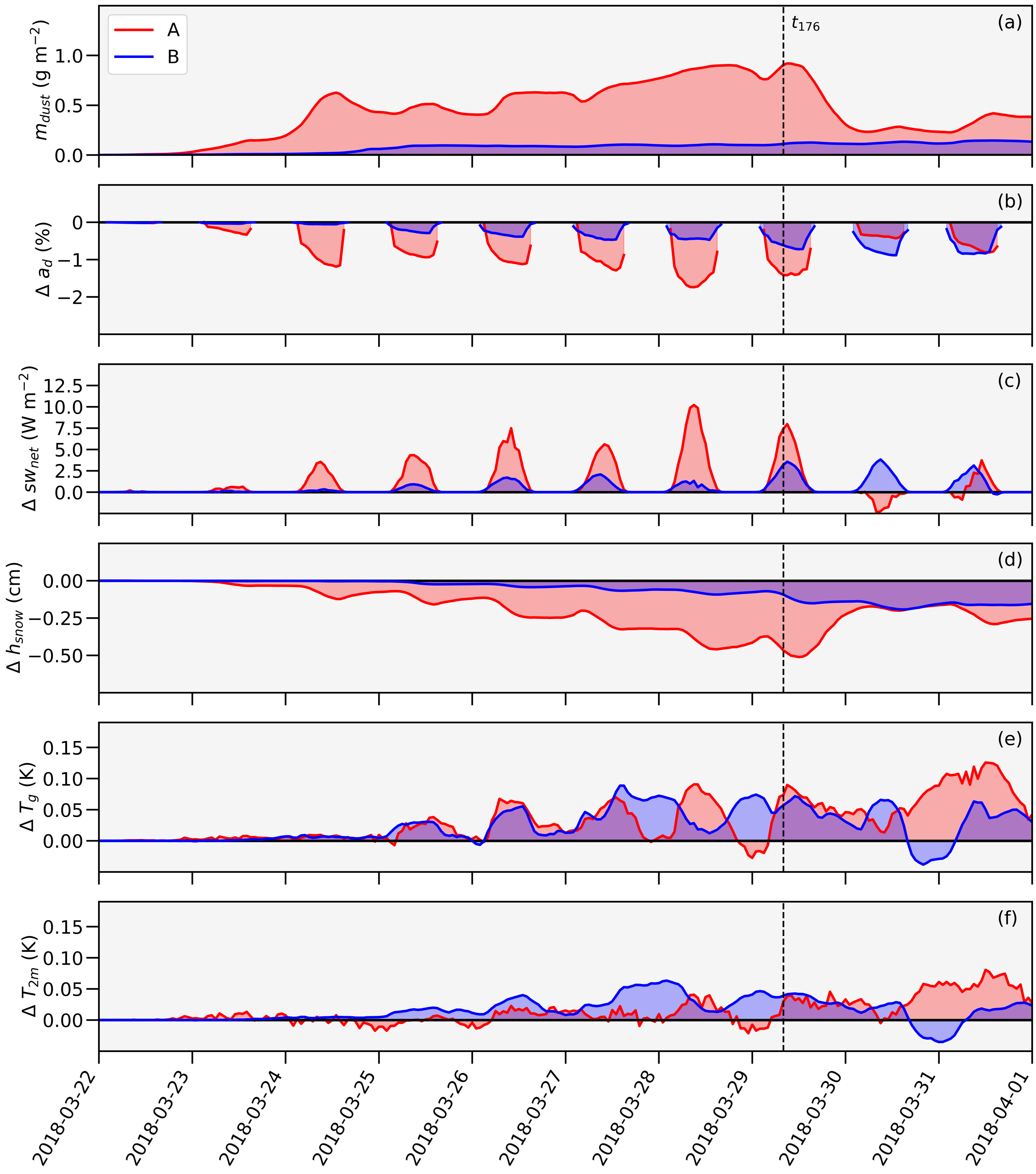
02\_Map\_dust\_event.png.



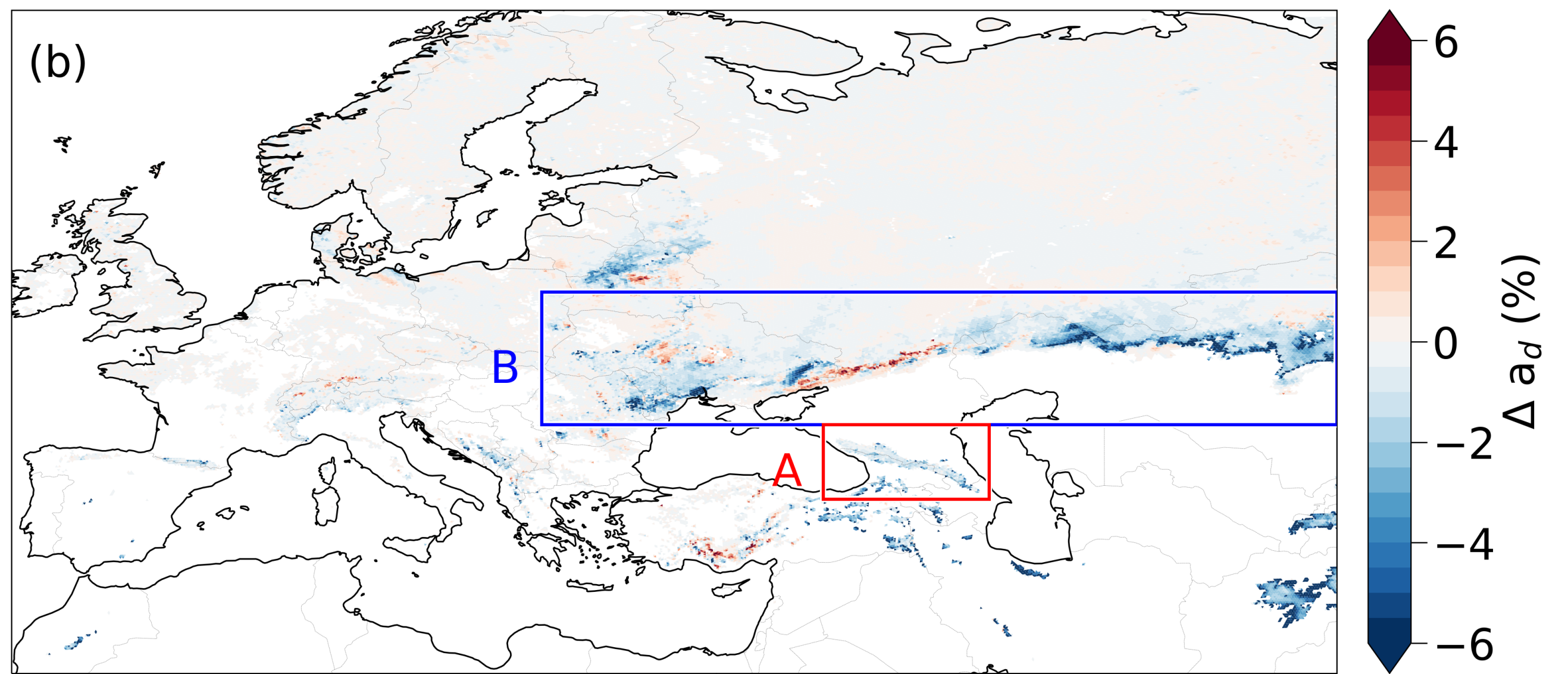
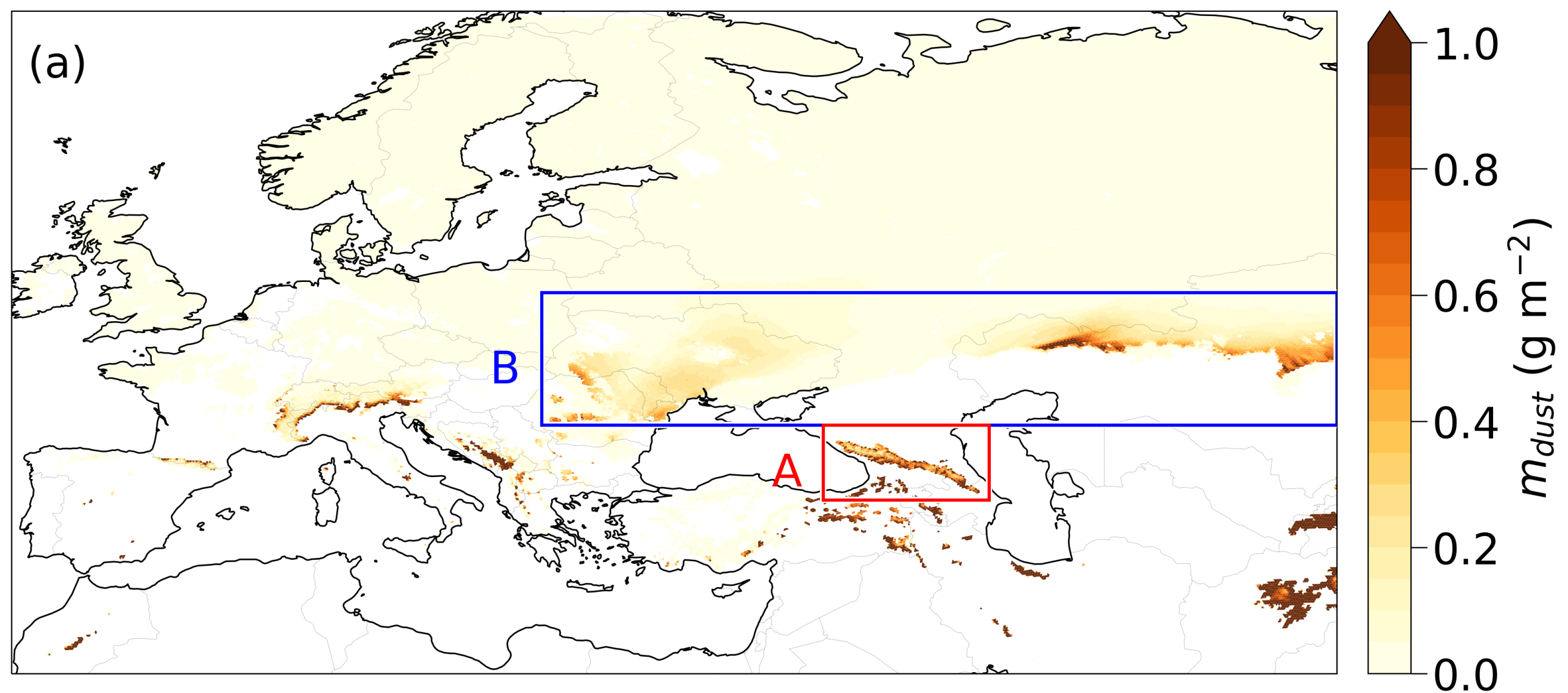
03\_CALIPSO-comparison\_attenuated\_backscatter.png.



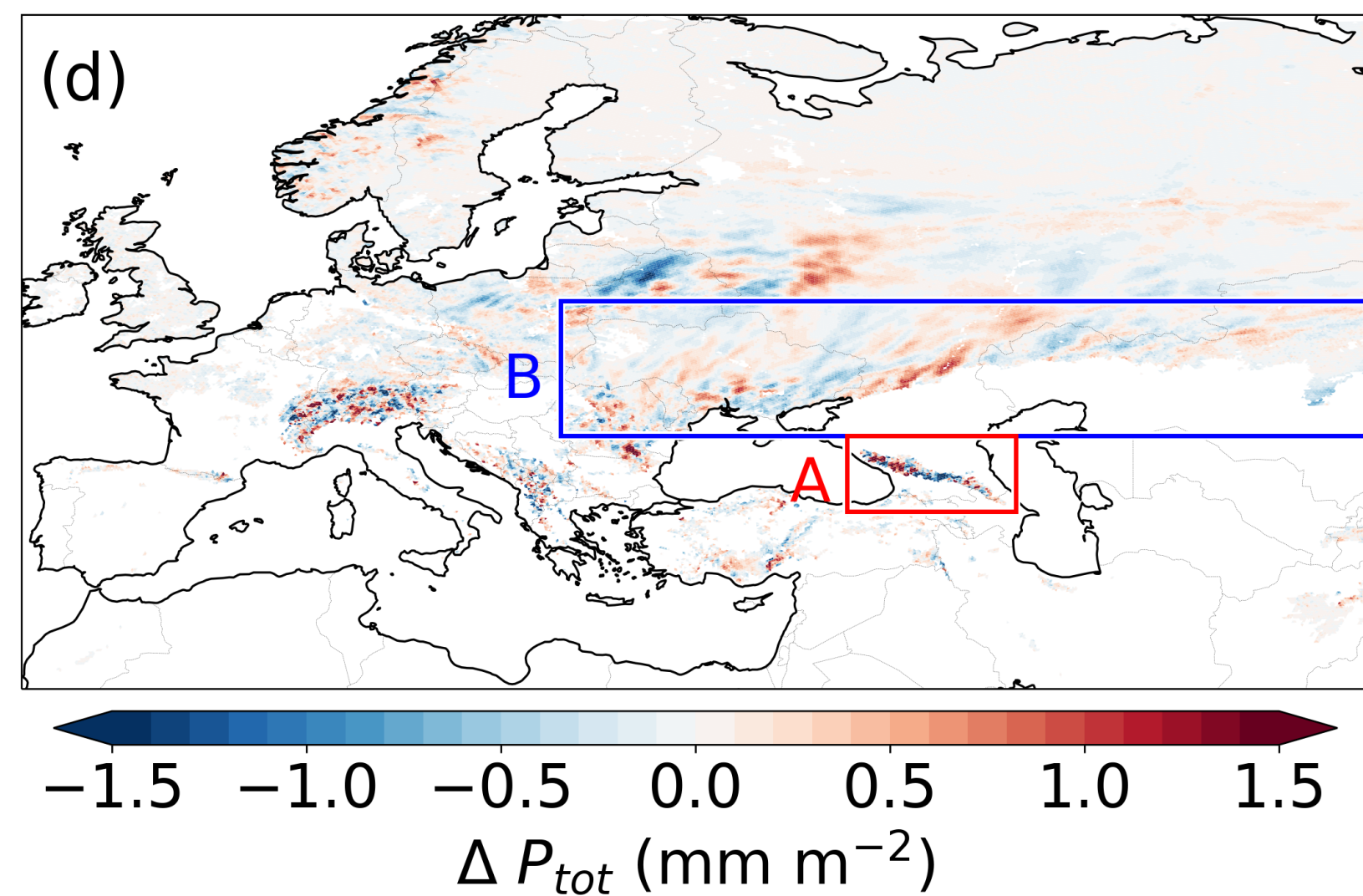
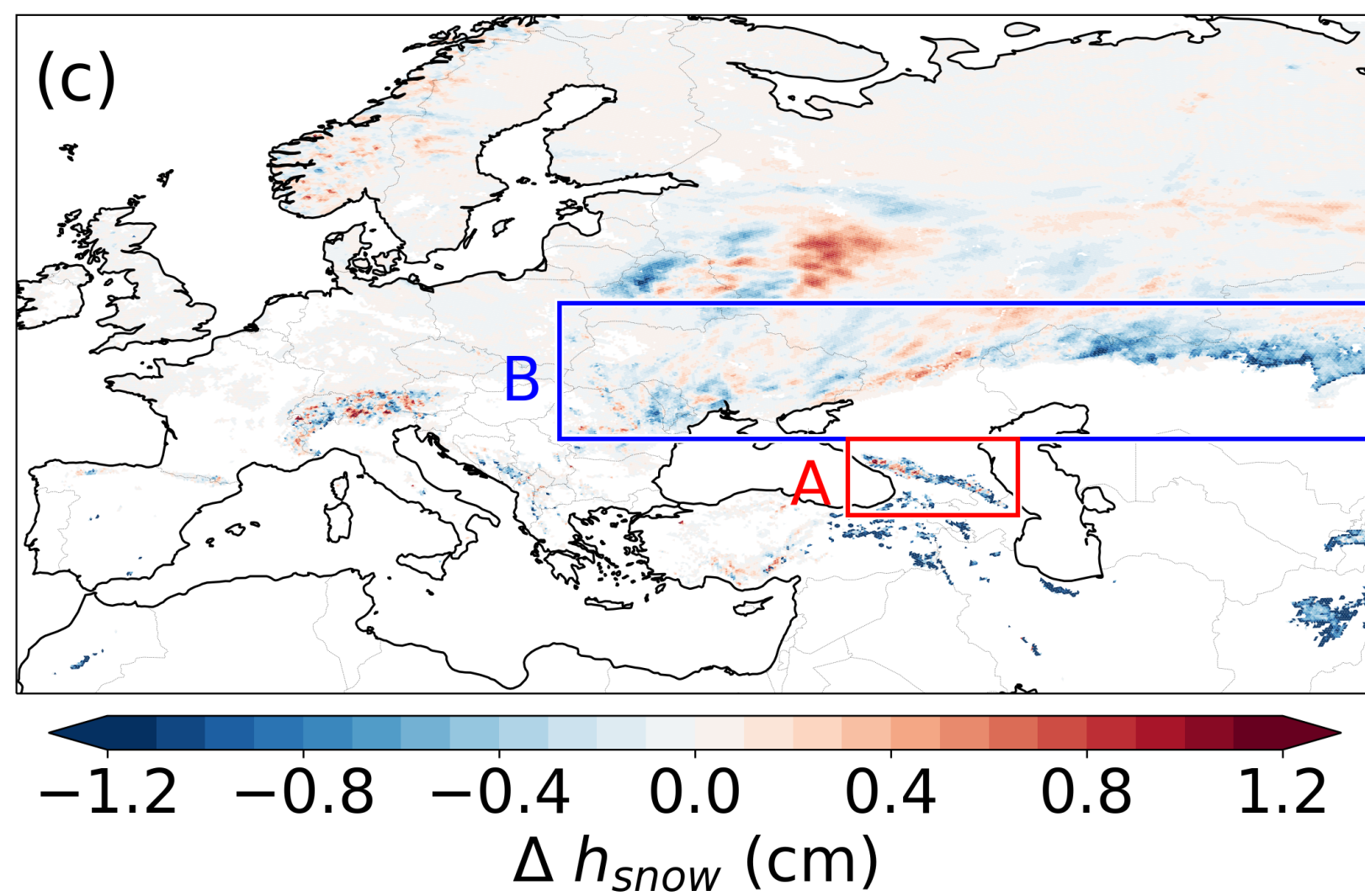
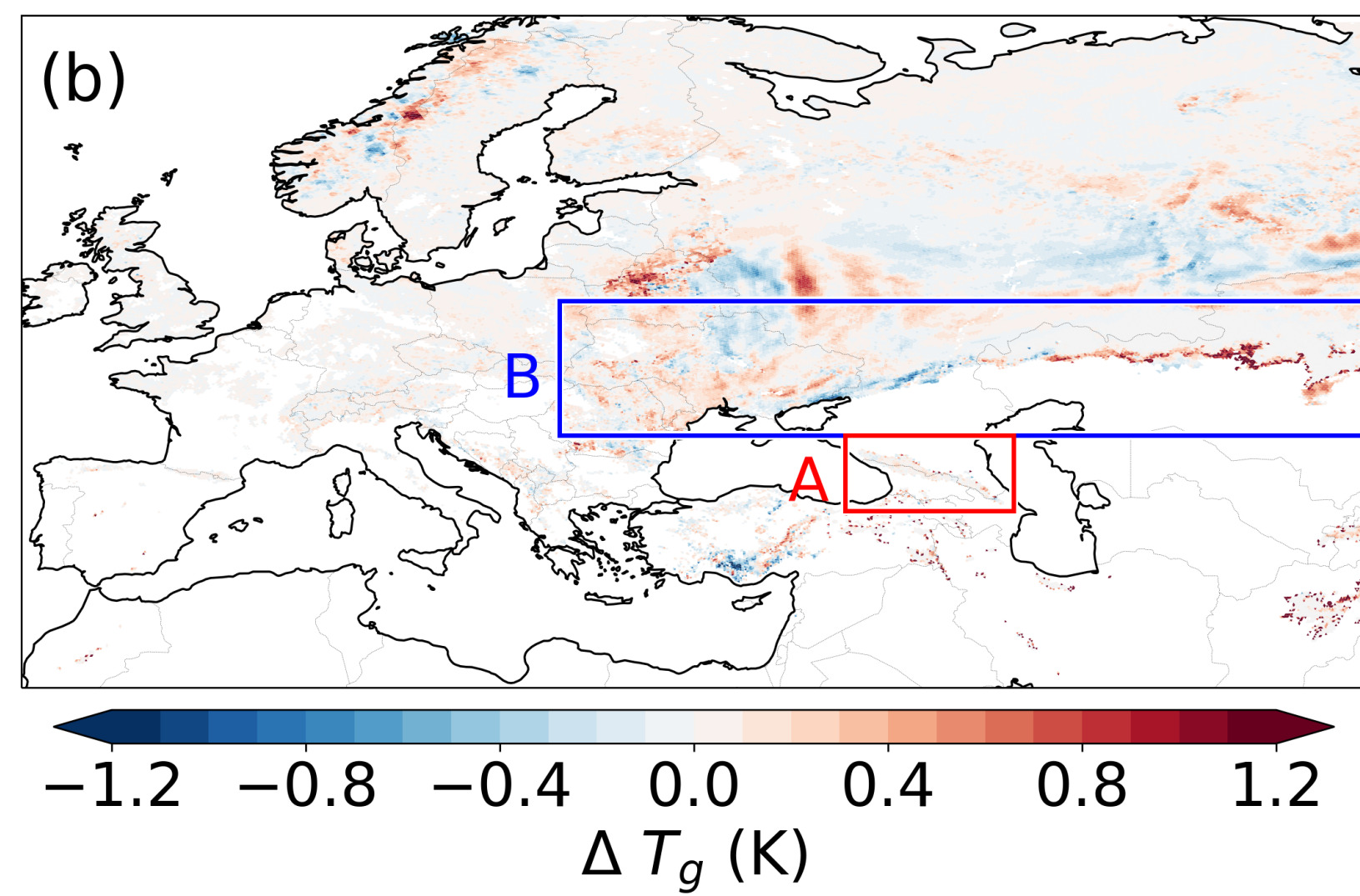
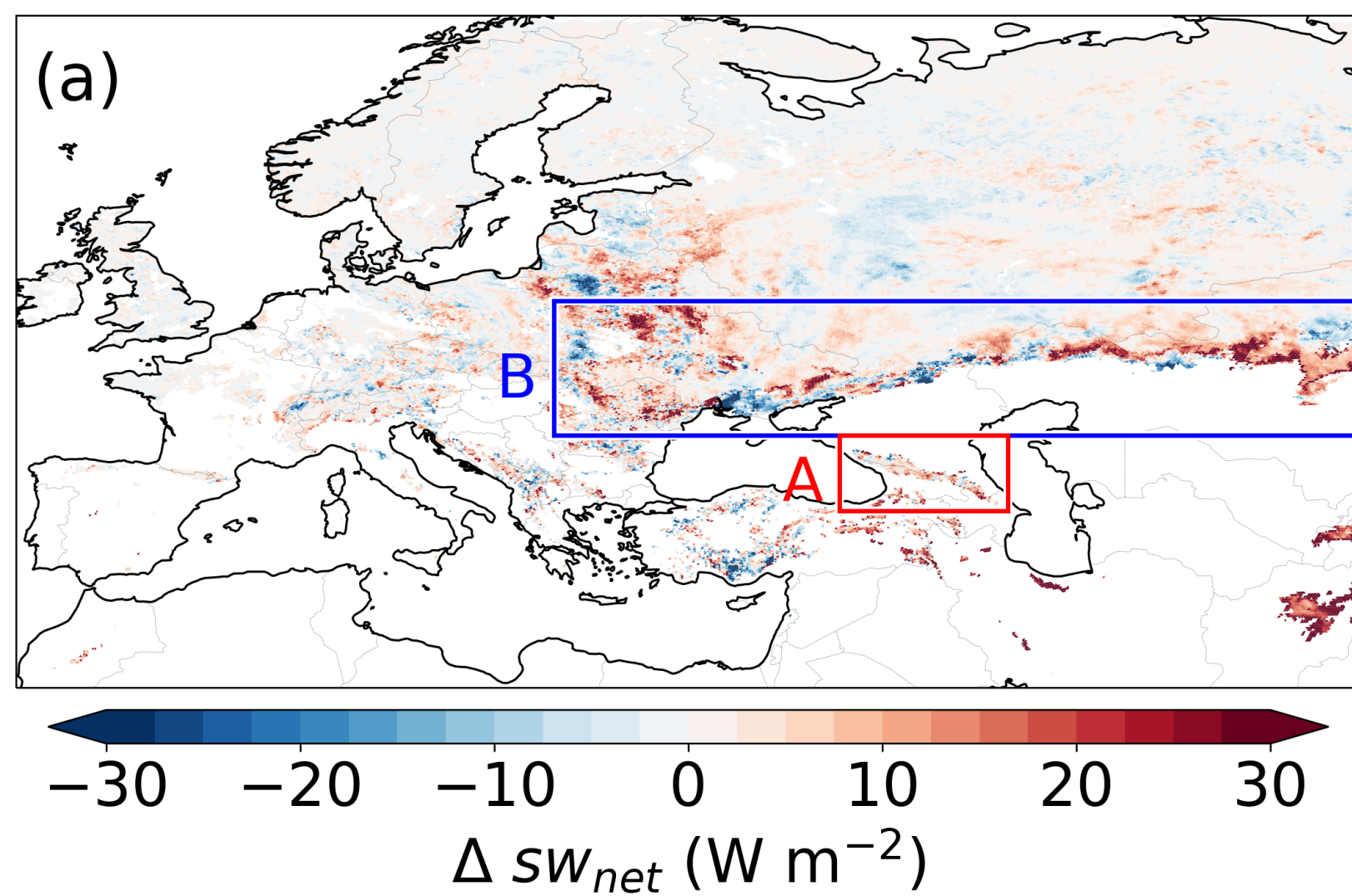
04\_SubDom\_time\_dust\_and\_snow.png.



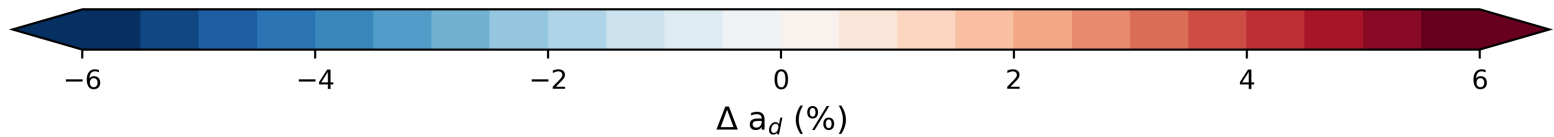
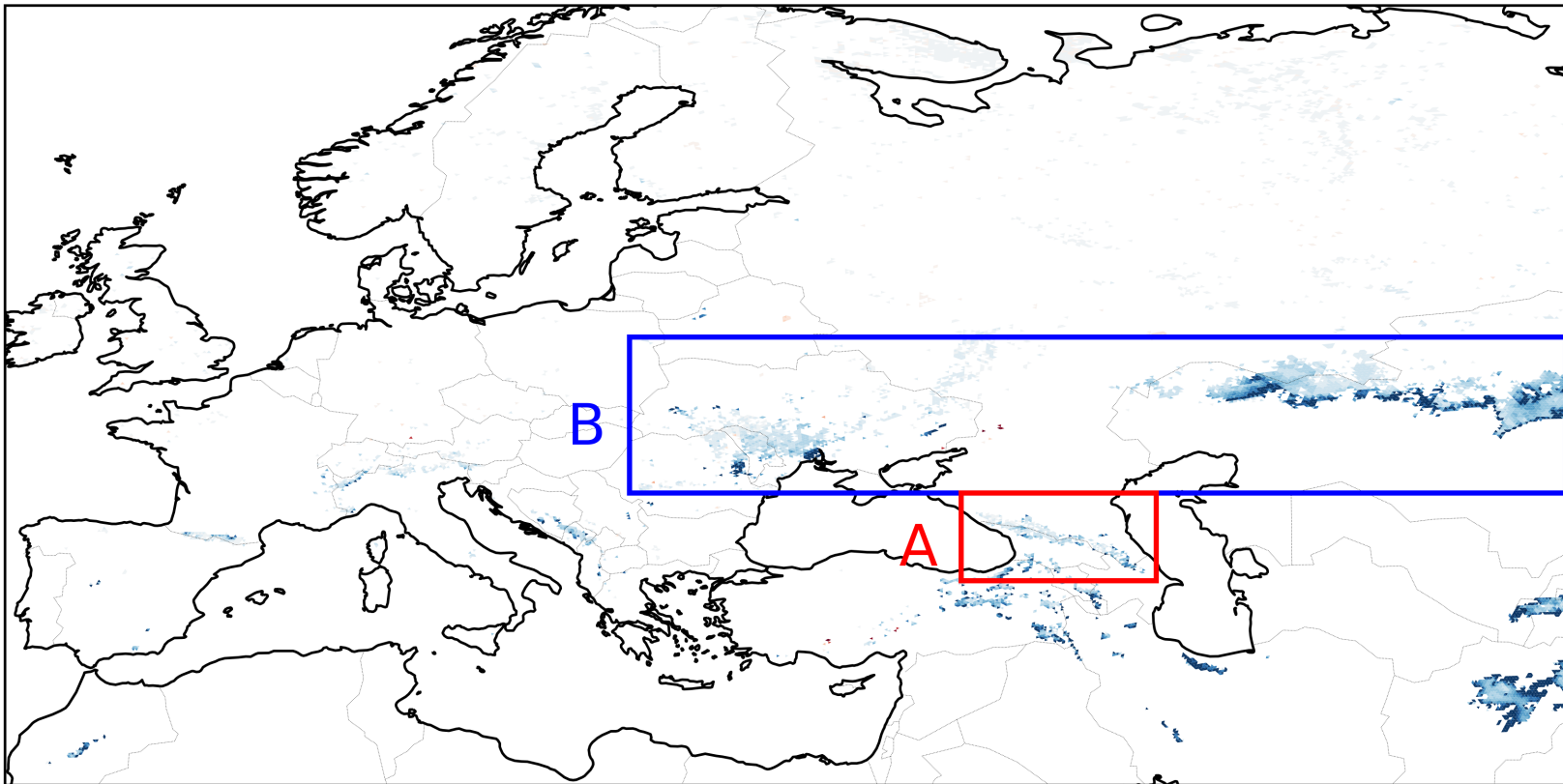
05\_EURASIA\_maps1.png.



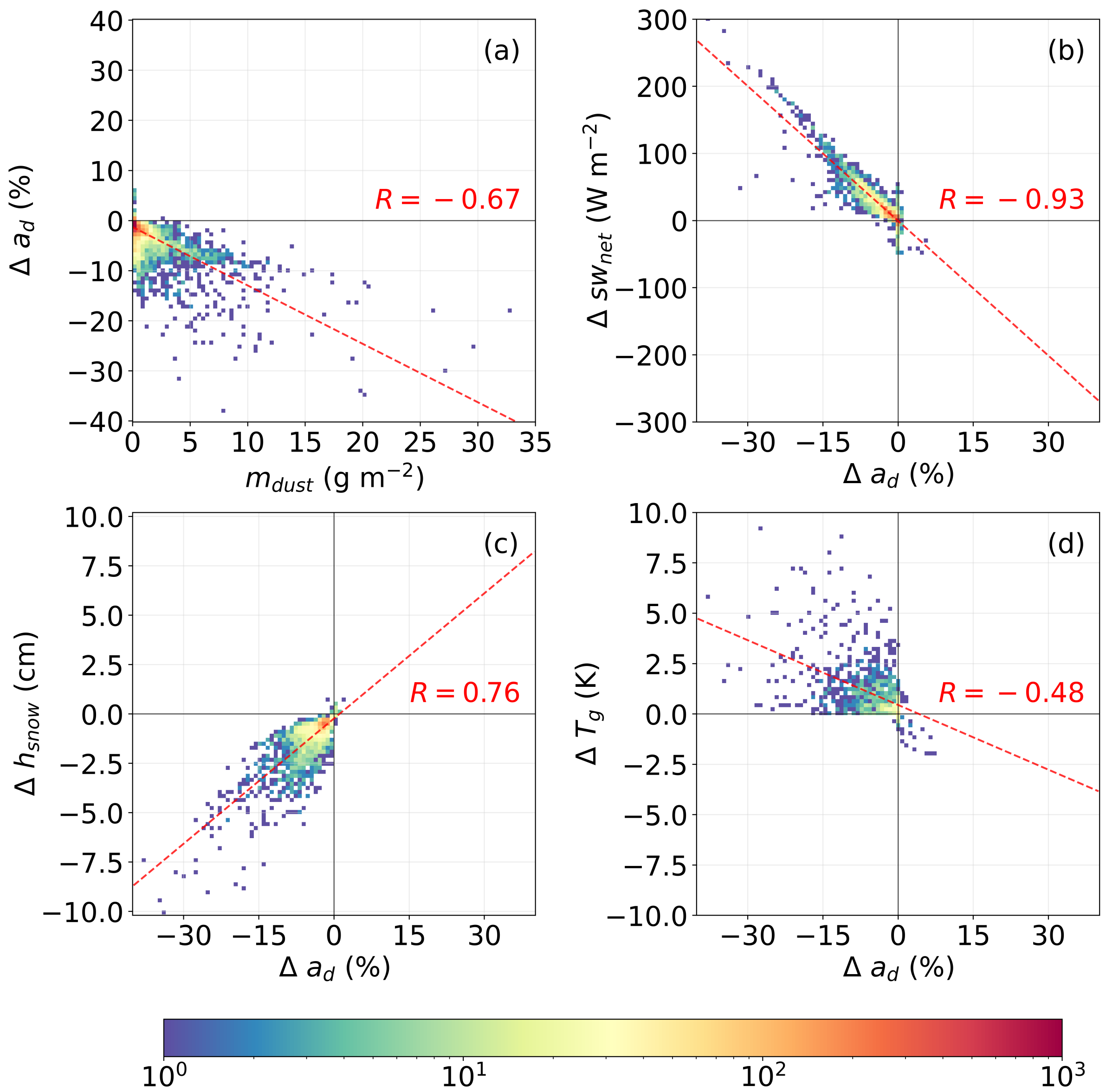
06\_EURASIA\_maps2.png.



07\_albdif\_significant.png.



08\_LAMDom\_sig\_hist.png.



09\_LAMDom\_sig\_hist\_hsnow.png.

